



# Ice thickness and water level estimation for ice-covered lakes with satellite altimetry waveforms and backscattering coefficients

Xingdong Li<sup>1,3</sup>, Di Long<sup>1,3</sup>, Yanhong Cui<sup>1,3</sup>, Tingxi Liu<sup>2,3</sup>, Jing Lu<sup>4</sup>, Mohamed A. Hamouda<sup>5,6</sup>, and Mohamed M. Mohamed<sup>5,6</sup>

<sup>1</sup>State Key Laboratory of Hydrosience and Engineering, Department of Hydraulic Engineering, Tsinghua University, Beijing 100084, China

<sup>2</sup>Water Conservancy and Civil Engineering College, Inner Mongolia Key Laboratory of Water Resource Protection and Utilization, Inner Mongolia Agricultural University, Hohhot 010018, China

<sup>3</sup>Collaborative Innovation Center for Integrated Management of Water Resources and Water Environment in the Inner Mongolia Reaches of the Yellow River, Hohhot 010018, China

<sup>4</sup>State Key Laboratory of Remote Sensing Science, Aerospace Information Research Institute, Chinese Academy of Sciences, Beijing 100101, China

<sup>5</sup>Department of Civil and Environmental Engineering, United Arab Emirates University, Al Ain 15551, United Arab Emirates

<sup>6</sup>National Water and Energy Center, United Arab Emirates University, Al Ain 15551, United Arab Emirates

**Correspondence:** Di Long (dlong@tsinghua.edu.cn) and Tingxi Liu (txliu1966@163.com)

Received: 26 June 2022 – Discussion started: 26 July 2022

Revised: 8 November 2022 – Accepted: 9 January 2023 – Published: 24 January 2023

**Abstract.** Lake ice, serving as a sensitive indicator of climate change, is an important regulator of regional hydroclimate and lake ecosystems. For ice-covered lakes, traditional satellite altimetry-based water level estimation is often subject to winter anomalies that are closely related to the thickening of lake ice. Despite recent efforts made to exploit altimetry data to resolve the two interrelated variables, i.e., lake ice thickness (LIT) and the water level of ice-covered lakes, several important issues remain unsolved, including the inability to estimate LIT with altimetric backscattering coefficients in ungauged lakes due to the dependence on in situ LIT data. It is still unclear what role lake surface snow plays in the retrieval of LIT and water levels in ice-covered lakes with altimetry data. Here we developed a novel method to estimate lake ice thickness by combining altimetric waveforms and backscattering coefficients without using in situ LIT data. To overcome complicated initial LIT conditions and better represent thick ice conditions, a logarithmic regression model was developed to transform backscattering coefficients into LIT. We investigated differential impact of lake surface snow on estimating water levels for ice-covered lakes when different threshold retracking methods are used. The developed LIT estimation method, validated against in situ data and

cross-validated against modeled LIT, shows an accuracy of  $\sim 0.2$  m and is effective at detecting thin ice that cannot be retrieved by altimetric waveforms. We also improved the estimation of water levels for ice-covered lakes with a strategy of merging lake water levels derived from different threshold methods. This study facilitates a better interpretation of satellite altimetry signals from ice-covered lakes and provides opportunities for a wider application of altimetry data to the cryosphere.

## 1 Introduction

Lake ice plays a unique and critical role in regulating lake ecosystems through the modulation of fluxes in and out of the lake, e.g., solar radiation, evaporation, sensible heat, and methane emission (Cooley et al., 2020; Engram et al., 2020; Sharma et al., 2019; Wang et al., 2018; Wik et al., 2016; Woolway et al., 2020). The vulnerability of lake ice to climate change causes wide concern for the stability of boreal lake ecosystems and the sustainability of socioeconomic activities that rely on lake ice (Knoll et al., 2019; Mullan et al., 2017). Lake ice cover and lake ice thickness (LIT) are two es-

sential climate variables (ECVs) related to lake ice identified by the Global Climate Observing System (GCOS). Lake ice cover is a measure of the lake ice quantity (horizontally). LIT can provide information on both the lake ice quantity (vertically) and quality (e.g., the strength of lake ice), which is highly related to the safety of human activities on ice. For instance, LIT loss could reduce the availability of ice roads (Li et al., 2022a) and increase the possibility of winter drowning (Sharma et al., 2020). However, compared with the intensively investigated lake/river ice cover (Du et al., 2017; Yang et al., 2020; Kropáček et al., 2013), the knowledge of LIT is largely limited, mostly due to the lack of in situ observations and effective remote-sensing-based methods. There is a considerable gap between the monitoring accuracy of LIT expected by the GCOS (1–2 cm) and that of current remote-sensing-based approaches (0.1–0.2 m). For winter water level estimation based on altimeters, the existence of lake ice is a barrier that could cause an abrupt decrease in the altimetric lake surface height (LSH; Shu et al., 2020). To resolve this issue, a better understanding of the impact of lake ice and lake surface snow on altimetric signals is necessary.

Current remote sensing of LIT is based mostly on information from thermal infrared sensors and microwave sensors (Murfitt and Duguay, 2021). Thermal infrared information such as lake surface temperatures can be used to drive a freezing degree-day-based model or more sophisticated lake ice models to estimate LIT (Yu and Rothrock, 1996; Pour et al., 2017; Zeng et al., 2016; Li et al., 2022a). However, cloud contamination and complex physical processes related to lake surface snow (Cheng et al., 2013; Duguay et al., 2003) could limit the accuracy and robustness of the method based on thermal infrared information and lake ice modeling. Microwave information has a certain penetration depth (Atwood et al., 2015) within the lake ice and is not affected by cloud cover, providing a great potential of more direct and robust observations of LIT.

Some previous studies focused on the use of passive microwave information, i.e., brightness temperature ( $T_B$ ) obtained by satellite radiometers. Kang et al. (2010) explored the relationship between  $T_B$  obtained by AMSR-E (Advanced Microwave Scanning Radiometer for EOS) and LIT in two Canadian lakes, Great Slave Lake (GSL) and Great Bear Lake (GBL), indicating that the increase in LIT is associated with the increase in  $T_B$ . They later showed that, with a linear regression model, a 18.7 GHz  $T_B$  could best represent the LIT accumulation, and the accuracy (root mean squared error, RMSE) was  $\sim 0.18$  m (Kang et al., 2014). Passive microwave methods perform well in terms of high temporal resolution (daily) but are limited to a few large lakes due to the low spatial resolution, as the pixel size of the 18.7 GHz  $T_B$  is 25 km.

Active microwave remote sensing of LIT can be further categorized into classes based on (1) synthetic-aperture radar (SAR) images or (2) satellite altimetry. Backscattering coefficients of SAR images would experience a rapid decrease

when the lake surface is covered by skim ice (a quasi-specular reflector), followed by a steady increase with the accumulation of LIT until the floating lake ice becomes bedfast lake ice or the melting starts (Duguay and Lafleur, 2003; Murfitt and Duguay, 2021; Howell et al., 2009a; Murfitt et al., 2018). Given the mentioned behaviors, backscattering coefficients from SAR images were widely used to discriminate bedfast lake ice from floating lake ice and the monitoring of lake/sea ice phenology (Howell et al., 2018, 2019). However, due to the high variability in the roughness associated with ice growth, the SAR-image-based LIT estimation is subject to larger uncertainty when the ice thickness exceeds 40 cm (Murfitt and Duguay, 2021).

Satellite altimeters were initially designed for monitoring ocean topography. Nevertheless, numerous studies have explored the potential of satellite altimetry in monitoring inland waters, such as river water levels and discharge, lake water levels and storage changes, glacier elevation changes and mass balance, and recently in LIT (Huang et al., 2019; Zakharova et al., 2021; Murfitt et al., 2022; Beckers et al., 2017; Zhang et al., 2021; Zhao et al., 2022; Li et al., 2022a; Huang et al., 2018; Li et al., 2019). Altimetry-based LIT can be derived from backscattering coefficients or radar waveforms. Different from the SAR images indicated above, backscattering coefficients from satellite altimeters would experience a rapid increase when the open water is covered with skim ice, followed by a steady decrease with the thickening of LIT until the melting starts. A recent study (Zakharova et al., 2021) investigated the relationship between the altimetry-based backscattering coefficients and in situ river ice thickness, suggesting the great potential of altimetry-based backscattering coefficients in estimating LIT for thin ice. However, in situ ice thickness data are necessary to derive regression models, which greatly limits applications of the method developed by Zakharova et al. (2021). To avoid confusion, the term “backscattering coefficients” refers to altimetry-based backscattering coefficients in the following context, unless otherwise stated.

LIT estimation based on satellite altimetric waveforms was first investigated by Beckers et al. (2017), with double-peak waveforms from CryoSat-2 on GSL and GBL, which provides a potential approach for robust LIT monitoring because the method is physically based and does not rely on parameterization. Shu et al. (2020) combined the method developed by Beckers et al. (2017) in winter water level retrieval using Sentinel-3 data. CryoSat-2 and Sentinel-3 are SAR altimeters with pulse-Doppler-limited footprints, which can be regarded as beam-limited footprints. Compared with traditional pulse-limited altimeters such as TOPEX/Poseidon (T/P) and Jason-1/2/3 (available since 1992), the time span of SAR altimeters such as CryoSat-2 and Sentinel-3 is relatively short (i.e., CryoSat-2 was launched in 2010, and Sentinel-3A was launched in 2016). The method developed by Beckers et al. (2017) is not that compatible with traditional pulse-limited altimeters because the waveforms of

pulse-limited altimeters are largely different from those from SAR altimeters. Li et al. (2022a) developed a LIT estimation method suitable for pulse-limited altimeters T/P and Jason-1/2/3. Therefore, the time span of retrievable LIT has been increased substantially from  $\sim 10$  years to almost 3 decades. The temporal resolution has also been largely improved because T/P and Jason-1/2/3 have the shortest revisit cycle ( $\sim 10$  d) among all existing satellite altimeters. However, the LIT estimation for thin ice based on radar waveforms is limited by the range resolution of the waveform. For instance, the minimum LIT retrievable with the method developed by Beckers et al. (2017) is 0.263 m for CryoSat-2 theoretically. For Jason-1/2/3, Li et al. (2022a) suggested that the LIT retrieval is robust after LIT exceeds 0.4 m because the waveforms of Jason-1/2/3 have a coarser range resolution than CryoSat-2.

Water level estimation for ice-covered lakes is essential for water resources management in the cryosphere under a changing climate (Li et al., 2022b; Long and Li, 2022; Wu et al., 2022) and has been investigated with different approaches for different altimeters (Shu et al., 2020; Yang et al., 2021; Ziyad et al., 2020). Ziyad et al. (2020) developed a classification scheme to separate Jason-2 observations from the ice-covered lake surface from the open-water surface and only used open-water observations to derive water level time series to avoid the contamination from lake ice. Shu et al. (2020) applied the method developed by Beckers et al. (2017) to estimate LIT using Sentinel-3 and then derived a range correction associated with LIT to correct the abrupt drop in winter altimetric water levels. Yang et al. (2021) tested several threshold retracking algorithms to develop a modified subwaveform threshold (MST) retracking method for two-peak waveforms from T/P and Jason-1/2/3 to improve the water level estimation during ice seasons. The MST retracking algorithm could avoid winter water level anomalies for most cases, and the metrics of derived altimetric water levels are quite promising, e.g., the standard deviations (SDs) of the differences between altimetric water levels and in situ water levels are mostly smaller than 0.1 m among study lakes (GSL, GBL, and Athabasca Lake). However, an important issue remains to be further discussed. Causes of the two-peak waveforms are still not clear and could be attributed to multiple backscattering surfaces, i.e., snow surface, snow–ice interface, and ice–water interface. Yang et al. (2021) suggested that the first subwaveform of Jason-1/2/3 waveforms from ice-covered lake surfaces corresponds to snow–ice interfaces based on the comparison with in situ water levels. However, Li et al. (2022a) suggested that the first subwaveform corresponds to the snow surface for most Canadian lakes based on the comparison with in situ ice and snow thickness. A better understanding of the formation of altimetry radar waveforms from ice-covered lake surfaces could benefit the retrieval of winter water levels and LIT.

This study was designed to (1) combine satellite-altimetry-based waveforms and backscattering coefficients to improve LIT estimation for ungauged lakes and thin ice and (2) explore possible improvements in altimetric water level estimation for ice-covered lakes through a better understanding of altimetric signals from snow and ice-covered lake surfaces. As mentioned above, LIT estimation based on waveforms alone is ineffective for thin ice, and altimetry-based backscattering coefficients have the potential to monitor thin ice. Meanwhile, the dependence on in situ data limits a wider application of altimetry-based backscattering coefficients to LIT estimation. Therefore, the combination of these two methods (satellite-altimetry-based backscattering coefficients and waveforms) could be complementary. To exploit the potential of backscattering coefficients in LIT estimation, we derived a logarithmic regression model to better represent various lake ice conditions, which is detailed in Sects. 3.2 and 4.1. As for water level estimation, we mainly explored different behaviors of lake surface snow when different threshold methods were used. We then developed an approach of merging water level time series derived from different threshold methods.

This paper is organized as follows. Section 2 introduces the study area and data used. Section 3 provides details on LIT estimation based on the combination of backscattering coefficients and waveforms from satellite altimetry, in addition to an improved water level estimation method for ice-covered lakes. Section 3 also includes a detailed deduction of an original logarithmic regression model used to convert backscattering coefficients into LIT. Section 4 shows the performance of the logarithmic model and the validation of LIT and water level estimation methods. Section 5 discusses differential impact of lake surface snow when different threshold methods are used, uncertainty sources of LIT estimation and water level retrieval, and implications of this study for future lake ice and lake water level research. Section 6 summarizes the main findings of this study.

## 2 Study area and data

### 2.1 Study area

As shown in Fig 1, we investigated eight lakes, including five lakes in Canada, i.e., GBL (121.30° W, 65.91° N), GSL (114.37° W, 62.09° N), Athabasca Lake (109.96° W, 59.10° N), Winnipeg Lake (97.25° W, 52.12° N), and Baker Lake (95.28° W, 64.13° N), as well as two lakes in Asia, i.e., Hulun Lake (117.38° E, 48.97° N) and Har Lake (93.21° E, 48.05° N), and one lake in Europe, i.e., Peipus Lake (27.45° E, 58.65° N). Environmental and climatic conditions of the study lakes are summarized in Table 1. GBL, GSL, and Athabasca Lake are located in the Mackenzie River basin, where mean annual temperature ranges from  $-10$  to  $3^{\circ}\text{C}$  from the northern to the southern part of the basin.

Mean annual precipitation in the Mackenzie River basin is 410 mm but ranges between 300 and 1000 mm from north-east to southwest (Howell et al., 2009a; Abdul Aziz and Burn, 2006). Baker Lake is located in the northeastern part of Canada, with an annual air temperature of  $-9.6^{\circ}\text{C}$  and an annual precipitation of 157 mm (Medeiros et al., 2012). Winnipeg Lake covers a wide range of latitudes, and mean annual air temperatures vary considerably from south ( $1.6^{\circ}\text{C}$ ) to north ( $-0.7^{\circ}\text{C}$ ). Mean annual precipitation in the Winnipeg Lake basin is 498 mm (Stewardship, 2011). Hulun Lake has an annual temperature of  $2.3^{\circ}\text{C}$  and an annual precipitation of 240 mm that mostly takes place from June to September due to a continental monsoon climate (Cai et al., 2016; Wu et al., 2019). Har Lake (Khar Lake) is located in a desert in Mongolia, with an annual temperature of  $\sim 0.8^{\circ}\text{C}$  and an annual precipitation of  $\sim 50$  mm based on reanalysis data and a surface water resource report ([https://raise.suiri.tsukuba.ac.jp/new/press/youshi\\_sugita8.pdf](https://raise.suiri.tsukuba.ac.jp/new/press/youshi_sugita8.pdf), last access: 19 January 2023). Peipus Lake is on the border of Russia and Estonia, with a mean annual temperature of  $\sim 6^{\circ}\text{C}$  and a mean annual precipitation of  $\sim 630$  mm, based on climate records from the Estonia Environment Agency (<https://www.ilmateenistus.ee/?lang=en>, last access: 19 January 2023). Among the eight study lakes, based on the availability of in situ measurements and environmental conditions, GSL, Baker Lake, Peipus Lake, Hulun Lake, and Har Lake were selected for testing the LIT retrieval method, while GSL, GBL, Athabasca Lake, and Winnipeg Lake were selected for the test of the water level estimation method.

## 2.2 Data

The satellite altimetry data we used here were collected by Jason-1/2/3, covering the 2002–2020 period. Ground tracks for each lake are shown in Fig. 1. Jason-1/2/3 are follow-on missions of T/P and inherited the orbit of their predecessor. T/P and Jason-1/2/3 have the shortest revisit time, of  $\sim 10$  d, among existing satellite altimetry missions, providing observations from  $66^{\circ}\text{N}$  to  $66^{\circ}\text{S}$ . Radar altimeters carried by Jason-1/2/3 are dual-frequency (Ku-band and C-band) pulse-limited altimeters. The term pulse-limited essentially means that the size of radar altimetry illuminated area/footprints is limited by the pulse width as opposed to the beam width (such as laser altimeters and SAR altimeters). As a result, the trailing edge of pulse-limited waveforms is milder and noisier than that of beam-limited waveforms, adding to the difficulty of retrieving LIT based on waveforms.

The altimetry products used here were the Sensor Geophysical Data Records (SGDRs), containing waveforms, backscattering coefficients for the Ku band and C band, satellite altitude, uncorrected range, and range corrections (atmospheric corrections and geophysical corrections) for 20 Hz footprints (20 footprints per second, with a spacing of  $\sim 330$  m). The SGDR products also provide corrected ranges using several retracking algorithms (ICE, MLE3, and MLE4)

**Table 1.** Environmental and climate conditions of study lakes.

Lake/region name	Mean air temperature ( $^{\circ}\text{C}$ )	Winter air temperature ( $^{\circ}\text{C}$ )	Precipitation (mm)	Location	Reference
Mackenzie River basin (GBL, GSL, Athabasca Lake)	$-10$ to $3$	$-35$ to $-25$	410	$\sim 115^{\circ}\text{W}$ , $\sim 62^{\circ}\text{N}$	Abdul Aziz and Burn (2006), Howell et al. (2009b)
Baker Lake	$-9.6$	$-30$ to $-20$	157	$95.28^{\circ}\text{W}$ , $64.13^{\circ}\text{N}$	<a href="https://climate.weather.gc.ca">https://climate.weather.gc.ca</a> (last access: 19 January 2023) and Medeiros et al. (2012)
Winnipeg Lake	$-0.7$ to $1.6$	$-20$ to $-5$	498	$97.25^{\circ}\text{W}$ , $52.12^{\circ}\text{N}$	<a href="https://climate.weather.gc.ca">https://climate.weather.gc.ca</a> (last access: 19 January 2023) and Stewardship (2011)
Hulun Lake	2.3	$-16$ to $-10$	240	$117.38^{\circ}\text{E}$ , $48.97^{\circ}\text{N}$	Wu et al. (2019) and Wang et al. (2017)
Har Lake	$\sim 0.8$	$-15$ to $-5$	$\sim 50$	$93.21^{\circ}\text{E}$ , $48.05^{\circ}\text{N}$	Mongolia surface water report and reanalysis data
Peipus Lake	$\sim 6$	$-5$ to $-2$	630	$27.45^{\circ}\text{E}$ , $58.65^{\circ}\text{N}$	<a href="http://www.ilmateenistus.ee">http://www.ilmateenistus.ee</a> (last access: 19 January 2023)

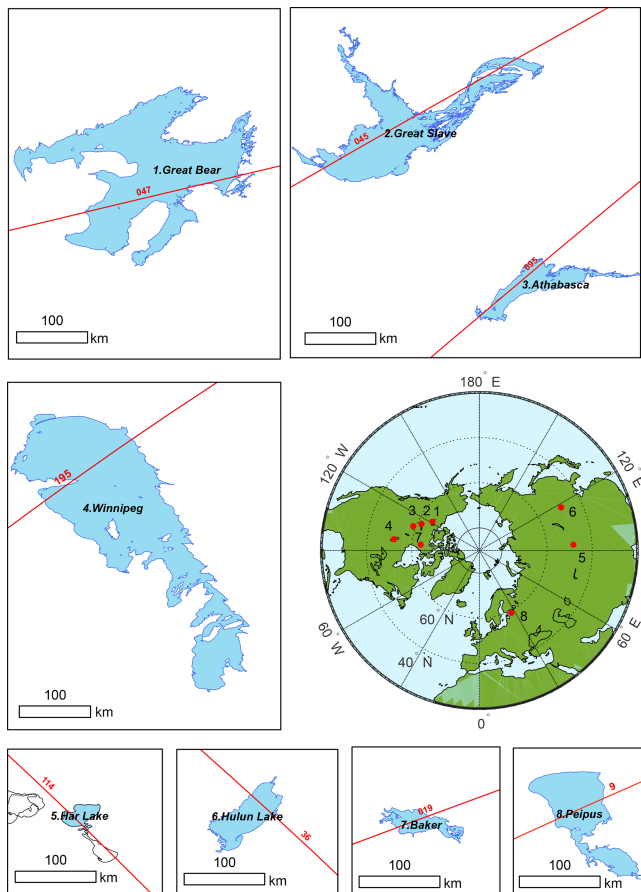


**Figure 1.** Study lakes and satellite altimetry ground tracks used. Red curves denote ground tracks of T/P and Jason-1/2/3. Red numbers denote the ground track number.

but have been shown to be unreliable in the water level estimation for ice-covered lakes (Yang et al., 2021). However, it does not mean that default retracking algorithms (MLE4) are irrelevant to this study. On the contrary, backscattering coefficients provided in the SGDR products are generated from the MLE4 retracking algorithm and are highly related to the amplitude of the waveforms. The altimetry data used can be obtained from the Archiving, Validation, and Interpretation of Satellite Oceanographic data (AVISO+; <http://ftp-access.aviso.altimetry.fr>, last access: 19 January 2023).

To validate the derived LIT, we obtained in situ LIT for GSL and Baker Lake collected by the Ice Thickness Program Collection, which is available at (<https://www.canada.ca/en/services/environment/weather/other-services.html>, last access: 19 January 2023). The data set contains weekly in situ snow and ice thickness measured with drilled holes. We also obtained in situ LIT of Lake Peipus from hydrological yearbooks of Estonia, which is available at (<https://www.ilmateenistus.ee/?lang=en>, last access: 19 January 2023). Sampling positions of GSL, Baker Lake, and Peipus Lake are listed in Table 2. It should be noted that in situ ice thick-

ness data are often measured near the shore, where the lake water freezes earlier, and the ice thickness could be larger at the beginning of ice seasons (Murfit et al., 2022; Mangilli et al., 2022). Data records for GSL and Baker Lake have been updated to 2016 and 2020, respectively. To validate the derived altimetric water levels, we obtained daily gauge water levels for GBL, GSL, Athabasca Lake, and Winnipeg Lake collected by the Water Survey of Canada (available at [https://wateroffice.ec.gc.ca/index\\_e.html](https://wateroffice.ec.gc.ca/index_e.html), last access: 19 January 2023). Gauge station names, station codes, locations, and record time span for different lakes are listed in Table 2. The in situ water levels were measured with pressure sensors and therefore represent the free water surface (Yang et al., 2021). Given that in situ and altimetric water levels are based on different datums, we removed the systematic bias between them before making any comparison. The systematic bias is defined as the mean difference between in situ water level time series and altimetric water level time series.

We also used modeled LIT to provide cross-validation for lakes without in situ LIT measurements. The modeled LIT data were based on a one-dimensional remote sensing lake ice model developed by Li et al. (2022a). The 1-D lake ice model developed by Li et al. (2022a) has a similar structure to the HIGHTSI (high resolution one-dimensional thermodynamic snow and ice) model, but it uses the Moderate Resolution Imaging Spectroradiometer (MODIS) Land Surface Temperature (LST) sensor as the upper boundary condition to solve the heat transfer equation within lake ice and surface snow. MODIS albedo was also incorporated to reduce uncertainty in simulated surface snow depth. Based on validation against in situ data (e.g., in Baker Lake, GSL, and Peipus Lake), the remote sensing lake ice model shows an accuracy of 0.1–0.2 m (RMSE). The modeled LIT is available at <https://doi.org/10.5281/zenodo.5528542> (Li et al., 2021).

### 3 Method

A workflow of the methods to retrieve LIT and LSH is illustrated in Fig. 2. Ku-band backscattering coefficients of Jason-1/2/3 were first extracted to classify the type of the observation, i.e., the open-water period and the ice-covered period. The LIT would first be estimated based on double-peak waveforms (to be illustrated in Sect. 3.1). Then the initial LIT results were used to derive a regression model with the Ku-band backscattering coefficients of Jason-1/2/3 to transform backscattering coefficients into LIT (to be explained in Sect. 3.2). Subsequently, the LITs based on waveforms and backscattering coefficients were merged and validated/cross-validated against in situ LIT/modeled LIT.

LSH estimation is based on threshold retracking methods (to be detailed in Sect. 3.3). For the double-peak waveform in the ice-covered period, only the first subwaveform is used to retrieve LSH, which is similar to what Yang et al. (2021) have done. Here we used different thresholds (0.1 and 0.5) to gen-

**Table 2.** In situ lake water level gauging stations and LIT observation sites used in this study.

Lake name	Data	Station ID	Location	Period of available records
Great Bear Lake (GBL)	Water level	10JE002	66.6° N, 117.6° W	10 Jul 1984–31 Dec 2018
Great Slave Lake (GSL)	Water level	07OB001	62.4° N, 114.35° W	31 Jan 1934–31 Dec 2018
	Ice thickness	/	62.4° N, 114.35° W	2 Jan 1992–28 Apr 2016
Winnipeg Lake	Water level	05SG001	53.18° N, 99.2° W	24 Jun 1953–31 Dec 2020
Athabasca Lake	Water level	07MC003	59.38° N, 108.88° W	25 Feb 1956–31 Dec 2020
Baker Lake	Ice thickness	/	64.3° N, 96.0° W	10 Jan 1992–31 Dec 2021
Peipus Lake	Ice thickness	/	58.83° N, 26.99° E	8 Jan 1991–25 Feb 2015

erate two LSH time series (LSH\_01 and LSH\_05 in Fig. 2) because they have different performance in open-water and ice-covered periods, i.e., the time series derived from a 0.1 threshold could better reveal the LSH for the ice-covered period, whereas that derived from a 0.5 threshold could better represent the LSH for the open-water period. The systematic bias between the two time series based on the 0.1 and 0.5 thresholds during the open-water period was removed to merge them into the final LSH time series that were validated with in situ water levels.

### 3.1 LIT retrieval with satellite altimetry waveforms

LIT estimation based on Jason-1/2/3 waveforms was developed by Li et al. (2022a). Here we provide the basic concepts and steps of this method and some comparisons with previous studies. Altimetry radar waveforms represent the returned radar power as a function of time. When the lake surface is covered with ice and snow, the radar pulse can be backscattered from the air–snow interface, the snow–ice interface, or the ice–water interface. The coupling of signals backscattered from different interfaces could result in the double-peak waveforms. The second peak of the waveform, often the highest, is related to the signal from the ice–water interface. However, the source of the first peak is still not clear. The time lag between the two peaks is the time a radar pulse transfers between the two interfaces and can be used to calculate the thickness of the medium. Beckers et al. (2017) tested the first peak and the highest peak of CryoSat-2 waveforms to estimate the LIT. SAR altimeters such as CryoSat-2 can be seen as beam limited in the along-track direction. The beam-limited waveforms have steep trailing edges so that it is easier to identify peaks associated with the ice–water interface. Nonetheless, for pulse-limited altimeters with a mild and noisy trailing edge, multiple peaks in the trailing edge are not uncommon, as shown in Fig. 3a, making it difficult to select the correct peak associated with the ice–water interface. In addition, LITs derived using waveform peaks are discrete because the time difference between different peaks is multiple integers of a bin width (3.125 ns for Jason-1/2/3). Therefore, Li et al. (2022a) developed a dual-threshold retracking algorithm to estimate the LIT with Jason-1/2/3 waveforms.

Procedures of the dual-threshold retracking method are as follows.

1. Find the inflection point  $T$  on the leading edge of the waveform. If the inflection point appears near the middle of the leading edge, then it indicates that there could be two peaks on the leading edge representing the snow/ice surface and ice bottom. If the inflection point appears close to the top of the leading edge, then it suggests that there is only one peak on the leading edge, and the waveform will be discarded. Assume that the waveform is comprised of  $P_1, P_2, \dots, P_N$ . The power difference for adjacent bins can be calculated as  $D_i = P_{i+1} - P_i$ .  $S$  is the SD of  $D_1, D_2, \dots, D_{N-1}$ . The first bin of the leading edge is defined as the  $G_0$ , which satisfies  $D_{G_0} > 0.2 \times S$ . Then  $[G_0, G_0+15]$  is defined as the search window. The inflection point  $T$  in the search window satisfies  $D_T < D_{T-1}$ . Subsequently, find the maximum power  $P_M$  in the search window. If  $P_T > 0.9P_M$ , discard the waveform, because the inflection point appears near the top of the leading edge.
2. The first subwaveform associated with the snow/ice surface is defined as  $[P_{G_0}, \dots, P_{T+1}]$ , while the second subwaveform associated with the ice bottom is defined as  $[P_T, \dots, P_M]$ . Then, two thresholds ( $Th_1$  and  $Th_2$ ) can be calculated to determine the two tracking points for the snow/ice surface and ice bottom. Here we used a 0.5 threshold to calculate  $Th_1$  and  $Th_2$ , as shown by Eqs. (1)–(2). The two tracking points ( $T_1$  and  $T_2$ ) can be calculated with Eqs. (3)–(4).

$$Th_1 = 0.5 \times (P_{G_0} + P_{T+1}) \quad (1)$$

$$Th_2 = 0.5 \times (P_T + P_M) \quad (2)$$

$$T_1 = x + \frac{Th_1 - P_x}{P_{x+1} - P_x}, \text{ where } P_x < Th_1, P_{x+1} > Th_1 \quad (3)$$

$$T_2 = y + \frac{Th_2 - P_y}{P_{y+1} - P_y}, \text{ where } P_y < Th_2, P_{y+1} > Th_2. \quad (4)$$

The ice thickness can be calculated as  $LIT = 0.5 \times (T_2 - T_1) \times c_i \times 3.125 \times 10^{-9}$ , where  $c_i$  is the speed of microwave in ice. The  $c_i$  is calculated with  $c/n_i$ , where  $n_i$  is 1.78, the refractive index of ice at the Ku band (War-



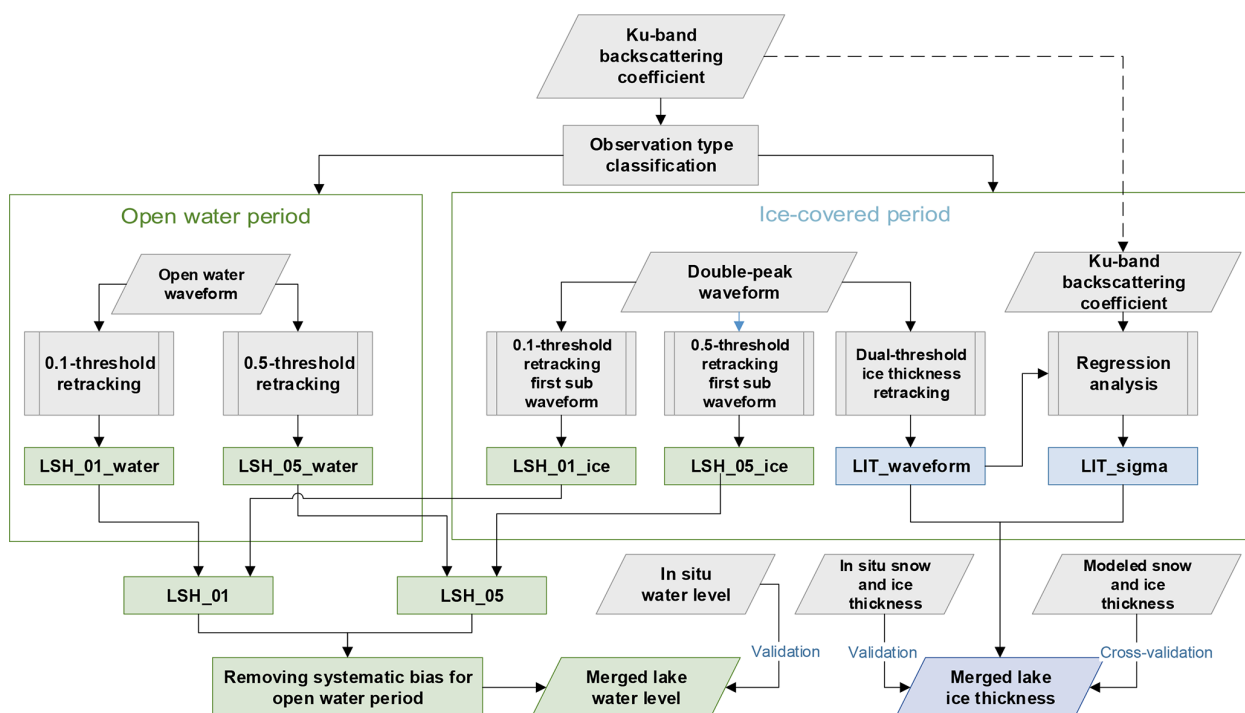


**Figure 2.** Workflow of this study. Procedures/intermediate data associated with LSH estimation are marked with green. Procedures/intermediate data associated with LIT estimation are marked with blue. LSH\_01\_water denotes that these intermediate data are the lake surface height (LSH) derived with a 0.1 threshold during the open-water period. LSH\_01\_ice denotes the same meaning but for the ice-covered period. LSH\_01 denotes the time series containing all LSH retrievals derived with a 0.1 threshold. Similarly, LSH\_05\_water, LSH\_05\_ice, and LSH\_05 denote the LSHs for different periods derived with a 0.5 threshold. LIT\_waveform denotes the LIT derived from double-peak waveforms. LIT\_sigma denotes LIT derived from backscattering coefficients.

ren and Brandt, 2008). After acquiring LITs for all footprints for each cycle, the median LIT of each cycle will be used to form the LIT time series.

### 3.2 LIT retrieval with satellite altimetry backscattering coefficients

The evolution in backscattering coefficients during ice seasons is complicated and very different between satellite altimetry and SAR images. For open water, altimetric backscattering coefficients are relatively low, ranging from 10 to 20 dB for different cycles. For the same cycle, the spatial variation in altimetric backscattering coefficients on the open water is small ( $< 1$  dB), as shown by the red curve in Fig. 4b. Overall, there are four stages of variations in backscattering coefficients with ice evolution during ice seasons (dashed line boxes in Fig. 4a). Stage I refers to the period when the lake starts to freeze and be covered by skim ice. During this stage, the altimetric backscattering coefficients soar to a high value in a year (e.g., the first dashed line box in Fig. 4a), which could be attributed to the quasi-specular reflecting effect of the smoothed lake surface. Meanwhile, the spatial variation in the altimetric backscattering coefficients

becomes relatively large (generally  $> 2$  dB), as shown by the blue curve in Fig. 4c.

In comparison, backscattering coefficients derived from SAR images experience high and low values due to wind-induced lake surface roughness for open-water periods (Horstmann et al., 2003, 2000) but decrease rapidly when the lake starts to freeze. The reason why the altimetric backscattering coefficients deviate from those based on SAR images is that altimetry data are nadir-looking observations, while most pixels in SAR images are side-looking observations (Fu and Cazenave, 2000; Peureux et al., 2022). Consequently, the incident direction is collinear (noncollinear) with the reflection direction for satellite altimetry (SAR images). Therefore, the backscattered energy is high (low) by the quasi-specular reflector for satellite altimeters (SAR images). In the following context, the term “backscattering coefficients” refers to altimetry-based backscattering coefficients.

During stage II, with the increase in LIT, the backscattering coefficients start to decrease steadily until the melting starts (e.g., the second dashed line box in Fig. 4a). The decrease in backscattering coefficients could be attributed to the increased absorption and volume scattering associated with the increased LIT. During stage III, when the melting begins, there will be an abrupt decrease in backscattering coefficients

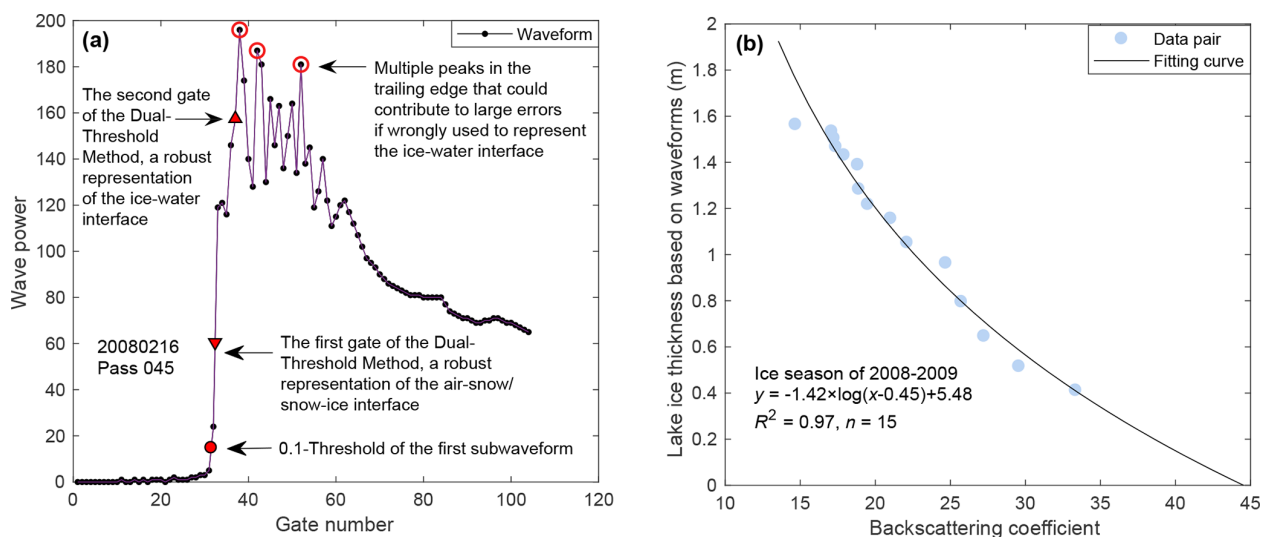


**Figure 3.** Mechanisms of the LIT estimation based on waveforms and backscattering coefficients. **(a)** A Jason-2 waveform obtained from ice-covered GSL. Red triangles indicate retracking points derived from the dual-threshold retracking algorithm, which can be used to estimate LIT. The red solid circle denotes the retracking point of the first subwaveform with a 0.1 threshold retracker, which can be used to derive LSH. **(b)** Scatterplot of the backscattering coefficients and LIT derived from the dual-threshold retracking algorithm through the ice season of 2008–2009 for GSL. Backscattering coefficients can be transformed into LIT with the derived regression model.

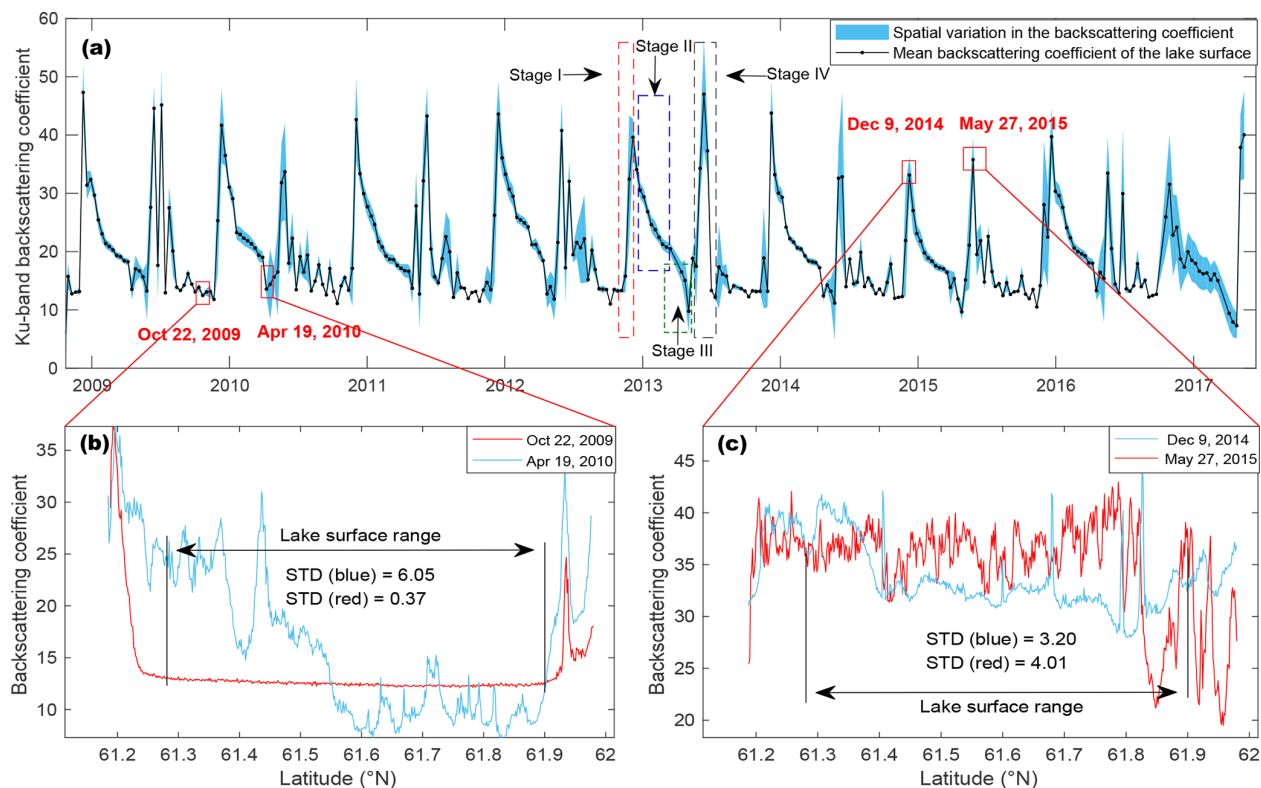


**Figure 4.** Temporal and spatial variations in the Jason-2 Ku-band backscattering coefficients on GSL. **(a)** Time series of mean backscattering coefficients for each cycle during 2009–2017. Blue shading areas denote the SD of backscattering coefficients for each cycle. Panels **(b)** and **(c)** are distributions of the backscattering coefficients along with latitudes for specific cycles/dates (including 22 October 2009 and 19 April 2010 in panel **b** and 9 December 2014 and 27 May 2015 in panel **b**). Lake surface latitudinal ranges are marked with double-arrows in panels **(b)** and **(c)**.



(e.g., the third dashed line box in Fig. 4a), which is caused partially by ice metamorphism (formation of dendroidal air channels just below the ice surface and early stages of needle ice formation; Kouraev et al., 2015). As shown by the blue curve in Fig. 4b, the backscattering coefficients are very low (e.g., < 10 dB) and noisy over the melting lake surface. The SD of the backscattering coefficients here representing the variability in the spatial domain for the melting period is much larger than that for the open-water period. Based on this phenomenon, we set a criterion (the mean backscattering coefficients < 15 dB and SD > 1.5 dB) to filter out the abrupt decrease in backscattering coefficients when the melting starts because these low values would lead to unrealistic large LIT estimates.

During stage IV, as the LIT continues to decrease with the melting process, backscattering coefficients start to increase to a high value once again because of the decrease in absorption and volume scattering effect. Eventually, once the ice completely melts, the backscattering coefficients drop to a level of the open-water surface (e.g., the fourth dashed line box in Fig. 4a). Therefore, the highest peak in the freezing period and the highest peak in the melting period were selected to characterize the ice-on and ice-off dates, which classify the observations into either open-water observations or ice-covered observations, as suggested by Zakharova et al. (2021). We compared the backscattered ice-on and ice-off dates against the ice phenology manually identified with MODIS images in GSL and found good agreement between the two independent data (Fig. S1 in the Supplement).

Based on the variability in backscattering coefficients during the ice seasons, Zakharova et al. (2021) assumed the decrease in backscatter between two consecutive observations to be proportional to the gain in ice thickness and derived a regression model between the cumulative backscatter difference and the in situ river ice thickness on the Lower Ob River. The regression model has the form of  $H_i = a \times \text{CumSum}(\text{dSig}/\text{dt})^b$ , where  $H_i$  is the ice thickness,  $\text{CumSum}(\text{dSig}/\text{dt})$  is the cumulative backscatter difference, and  $a$  and  $b$  are model parameters calibrated against in situ ice thickness. For simplicity, this model is referred to as the power function model in the following context. The power function model does not consider the physical process associated with ice growth and is dependent on in situ measurements, which limits a wider application of the method. In addition, we found that the performance of LIT estimation using only one regression model with one set of model parameters can be fairly unstable from year to year and from lake to lake, partially because the initial ice and snow conditions can be very different for each winter and each lake, which is also mentioned by Zakharova et al. (2021).

We developed a new regression model considering the physical processes and applied this model to relate backscattering coefficients with LITs derived from waveforms for each lake and during each winter. Therefore, we can circumvent the problems caused by the difference in initial ice

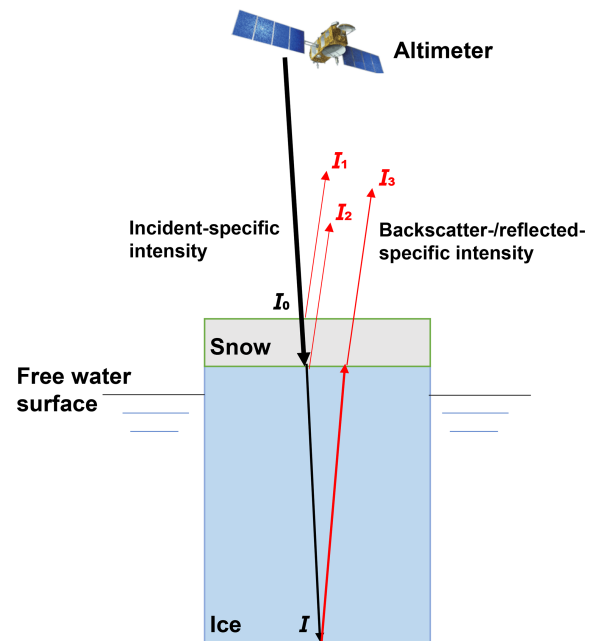


**Figure 5.** A schematic diagram of radar-altimetry-specific intensity backscattered/reflected from ice-covered lakes. Black arrows denote the incident-specific intensity. Red arrows denote backscattered- or reflected-specific intensity.  $I_0$  denotes the transmitted microwave intensity just below the snow–ice interface.  $I$  denotes the transmitted microwave intensity that has just reached the ice–water interface.  $I_1$  denotes the backscattered intensity from the air–snow interface,  $I_2$  denotes the backscattered intensity from the snow–ice interface, and  $I_3$  denotes the backscattered intensity from the ice–water interface. Note that, at the nadir, the incident angle is small, and the backscattered/reflected pulse is approximately collinear with the incident radar pulse.

and snow conditions. Meanwhile, we can derive LITs based on backscattering coefficients without in situ ice thickness measurements. Because our model has a logarithmic form (Eq. 10), it is referred to as the logarithmic model. As shown in Sect. 4.1, the logarithmic model can better represent the LIT compared with the power function model for lakes with thick ice (e.g., > 1 m) and rapid ice accumulation rates.

Theoretically, radar pulse would be backscattered from multiple snow and ice layers, given that different snow/ice layers have different density and temperatures that could influence the backscattering process. The backscattered intensity is a function of the distance, direction, and time that requires detailed modeling, as was done by Larue et al. (2021). To provide a straightforward derivation of the regression model we developed, here we focus on the backscattered intensity of the nadir and assume the radar pulse to be backscattered mostly from three interfaces, i.e., the air–snow interface, the snow–ice interface, and the ice–water interface. Volume scattering from snow layers also affects the backscattered intensity, which is discussed in Sect. 5.2. Here we approximate the backscattered intensity  $I_b$  with the sum of

$I_1$ ,  $I_2$ , and  $I_3$ , i.e., the backscattered intensity from the air–snow, the snow–ice, and the ice–water interfaces, as shown in Fig. 5. We assume the reflectance for these interfaces to be  $R_1$ ,  $R_2$ , and  $R_3$ , respectively. Given the incident intensity  $I_0$ , the backscattered intensity  $I_b$  can be written as Eq. (5):

$$I_b = I_1 + I_2 + I_3 = R_1 I_0 + I_2 + I_3. \quad (5)$$

At stage II (shown in Fig. 4), backscattering coefficients decrease with the increase in LIT, which could be caused by the increased absorption and volume scattering. Here we approximate the extinction of microwave intensity in snow and ice with an exponential equation. For instance,  $I_2$  and  $I_3$  can be written as Eqs. (6) and (7):

$$I_2 = R_2(1 - R_1)I_0 \times e^{-2kH_s} \quad (6)$$

$$I_3 = R_3(1 - R_2)(1 - R_1)I_0 \times e^{-2k(H_s+H_i)}, \quad (7)$$

where  $k$  is an effective extinction coefficient for snow and ice,  $H_s$  and  $H_i$  denote the thickness of snow and ice, and  $R_2$  and  $R_3$  denote reflectance at the snow–ice and the ice–water interfaces.

Note that the backscattered intensity does a round trip in the snow and ice. Therefore, the exponential term in Eq. (7) is written as  $\exp(-2k(H_s + H_i))$ . By substituting  $I_2$  and  $I_3$  in Eq. (5), the total microwave intensity backscattered from the ice-covered lake surface can be approximated by Eq. (8).

$$I_b = \left( R_1 I_0 + R_2(1 - R_1)I_0 \times e^{-2kH_s} \right) + R_3(1 - R_2)(1 - R_1)I_0 \times e^{-2k(H_s+H_i)}. \quad (8)$$

Based on Fresnel's equation, the reflectance of the interface is proportional to the difference in refractive indices. The differences in refractive indices of the air–snow and the snow–ice interfaces are relatively small compared with those of the ice–water interface, i.e.,  $R_1$  ( $I_1$ ) and  $R_2$  ( $I_2$ ) are relatively small compared to  $R_3$  ( $I_3$ ). Given that  $I_1$  and  $I_2$  are small and are not related to the ice growth, we use a constant to represent them in the model. The backscattering coefficients should be proportional to the backscattered intensity  $I_b$ . Therefore, we suggest using Eq. (9) to relate backscattering coefficients with the snow and ice thickness, as follows:

$$\sigma_0 = A + B \times e^{-K(H_s+H_i)}, \quad (9)$$

where  $\sigma_0$  is the backscattering coefficient, and  $A$ ,  $B$ , and  $K$  are model parameters to be calibrated. The following strategy can be used to determine the parameters in an efficient way. Parameter  $A$  generally ranges from 0 to 20 dB and is not very sensitive. Therefore, discrete values can be assigned to  $A$  directly, such as 0, 1, ..., 20. Then, for each assigned parameter  $A$ , transforming Eq. (9) into Eq. (10) results in the following logarithmic regression model:

$$(H_s + H_i) = -\frac{1}{K} \times \ln(\sigma_0 - A) + C, \quad C = \frac{\ln(B)}{K}, \quad (10)$$

where parameters  $K$  and  $C$  in Eq. (10) can be determined using linear regression. The residual sum of squares for each set of  $A$ ,  $K$ , and  $C$  can be calculated, and the parameter group with the lowest residual sum of squares was selected as the final estimates. The calibrated parameters are generally satisfactory, as shown in Fig. 3b. It is possible that the regression model yields negative LIT at the beginning of the ice seasons because the initial backscattering coefficient exceeds the range of data used in the regression. If that is the case, Eq. (9) can be adjusted as Eq. (11) to ensure that the initial LIT is non-negative, where  $\sigma_{\max}$  is the maximum backscattering coefficient during that ice season.

$$\sigma_0 = A + \sigma_{\max} \times e^{-K(H_s+H_i)}. \quad (11)$$

### 3.3 Water level estimation for ice-covered lakes

Yang et al. (2021) developed a straightforward method to retrieve water levels for ice-covered lakes using T/P and Jason-1/2/3 data. The basic concept of their method is to extract the first subwaveform from the double-peak waveform and apply the 0.1-threshold retracking algorithm to the first subwaveform. By comparing with in situ water levels, lake ice thickness, and snow depth, Yang et al. (2021) suggested that the first subwaveform retracked with a 0.1 threshold (e.g., the red circle in Fig. 3a) is associated with the snow–ice interface and can be used as a good approximation to the free water surface. We noticed that, in the dual-threshold retracking algorithm (Li et al., 2022a), the first tracking gate (e.g., the first red triangle in Fig. 3a) is very close to the 0.5-threshold tracking point of the first subwaveform. By comparing the altimetric LIT with in situ LIT and snow depth, we found that the altimetric LIT is close to the total thickness of ice and snow for most cases, meaning that the first tracking gate is likely associated with the snow surface. Consequently, it remains a question as to whether the first subwaveform represents signals from the snow surface or the snow–ice interface.

In addition, for a given waveform (as shown in Fig. 3a), the 0.1-threshold tracking gate (red circle) should be ahead of the 0.5 tracking point (the first red triangle), meaning that the associated surface height of the 0.1 threshold should be higher than that of the 0.5 threshold. But, based on the mentioned two studies, the 0.1 threshold is related to the snow–ice interface, while the 0.5 threshold is related to the snow surface. The inconsistency between the two studies causes ambiguity in determining the interface associated with the first subwaveform, thereby reducing the reliability of altimetric LIT and LSH for ice-covered lakes.

LSHs for ice-covered lakes were first retrieved using different thresholds. The 0.1 threshold yields higher LSH than the 0.5 threshold for each waveform, meaning that a systematic bias exists between LSH time series from the 0.1 threshold and from the 0.5 threshold. To remove the systematic biases, we selected LSH retrievals during open-water periods as the baseline because observations obtained dur-

ing open-water periods are more stable and robust. For the open-water period, the classic 0.1- and 0.5-threshold methods were directly applied to the waveform separately. During the ice-covered period, the 0.1- and 0.5-threshold methods were applied to the first subwaveform. All LSH retrievals for both ice-covered and open-water periods derived with the 0.1 threshold were aggregated into one time series (LSH\_01), and all LSH retrievals based on the 0.5 threshold were aggregated into the other (LSH\_05).

Subsequently, the systematic biases (bias) between the two time series were calculated as the mean difference between LSH\_01 and LSH\_05 during open-water periods. Then we combined the two time series by the concatenation of observations from LSH\_05 during open-water periods and those from (LSH\_01-bias) during ice-covered periods, yielding the merged LSH time series for the entire study period. In Sect. 4.3, we show that the merged time series outperformed both LSH\_01 and LSH\_05.

## 4 Results

### 4.1 Performance of the logarithmic regression model

To evaluate the performance of the logarithmic model, we proposed (Eq. 10) to convert backscattering coefficients into LIT. We compared it with the power function model used by Zakharova et al. (2021). As we mentioned in Sect. 3.2, our method can use waveform-based LIT to calibrate parameters in the logarithmic model and does not rely on in situ LIT. However, to evaluate the feasibility and potential of both models, we directly used in situ LIT in Baker Lake instead of waveform-based LIT to generate model parameters, which could represent the best performance of both models ideally. In addition, different from Zakharova et al. (2021), who split in situ data into training and validation periods, we used all available data in each ice-covered season to calibrate parameters for both models due to the large variability in optimal parameter sets in different ice-covered seasons.

As illustrated in Sect. 3.2, the power function model assumes the LIT to be a power function of the accumulated backscattering difference. The LIT naturally starts from zero on the freeze-up date detected by Jason-1/2/3 because the accumulated backscattering difference is zero at the beginning. It has been shown that the power function model is effective for the estimation of river ice thickness thinner than 1 m. But it is not clear if it is suitable for thicker ice conditions, e.g., in Baker Lake.

The maximum LIT in Baker Lake exceeds 2 m and, for most of the frozen season, the LIT is over 1 m, which means that the LIT would increase rapidly at the beginning of ice seasons. Therefore, when Jason-1/2/3 first detects the lake ice in their 10 d revisit cycles, the LIT is not zero but could be several decimeters, which is not fully considered in the power function model. The logarithmic model, however, is

compatible with such kind of initial LIT conditions, as shown by Fig. 6. It is obvious that, for the power function model, the initial LIT is estimated as zero, but in situ measurements could range from 0.2 to 1 m (Fig. 6a).

The logarithmic model could well represent the initial LIT, and its overall performance ( $R^2$  of 0.90 and RMSE of 17 cm) is better than that of the power function model ( $R^2$  of 0.77 and RMSE of 25 cm), even if the initial LIT data pairs are removed from the power function model ( $R^2$  of 0.78 and RMSE of 22 cm). In addition, underestimation of LIT is more severe in the power function model when the LIT exceeds 1.5 m, suggesting some saturation effects. Therefore, we suggest to using logarithmic models when the LIT exceeds 1 m or the LIT increases rapidly at the beginning of ice seasons.

### 4.2 LIT based on the combination of waveforms and backscattering coefficients

The accuracy of waveform-based LIT has been reported to be 0.15–0.2 m, based on a comparison against in situ data (Li et al., 2022a). The waveform-based LIT data set used in this study is available online (<https://doi.org/10.5281/zenodo.5528542>, Li et al., 2021). Here we mainly validated backscattering-coefficient-based LITs against the in situ thickness of lake ice and snow (Fig. 7). The overall performance of the backscattering-coefficient-based LIT is close to that based on waveforms, as summarized in the Table 3. Correlation coefficients (CCs) and RMSEs for Baker Lake, GSL, and Peipus Lake are 0.94, 0.80, and 0.76 and 24 cm, 17 cm, and 11 cm, respectively. As suggested by Zakharova et al. (2021), such accuracy is applicable in climate studies but may not meet the need for engineering purposes (e.g., ice roads).

The backscattering-coefficient-based LITs using our method show metrics slightly lower than that of Zakharova et al. (2021; RMSE of 7–18 cm). However, the relative errors between the two studies are similar because the ice thickness in the previous study (Zakharova et al., 2021) is generally smaller than 0.8 m, while the LIT and snow thickness on GSL and Baker Lake could be over 1.5 and 2 m, respectively. On the other hand, our method does not depend on in situ data and can be applied to ungauged lakes without in situ LIT measurements but with altimetric data. As we illustrated in Sect. 3.2, parameters used to convert backscattering coefficients into LIT can be calibrated against waveform-based LIT. The backscattered LIT shown in Figs. 7 and 8 was generated solely based on altimetry information. Calibration parameters and metrics for each lake and each ice season are available in the Supplement (Table S1).

The backscattered LIT has advantages in estimating thin ice, albeit based on parameters calibrated against waveform-based LIT. In Peipus Lake, where the total thickness of snow and ice does not exceed 0.8 m, the waveform-based method can only retrieve the LIT at the very late phase of ice accumulation, resulting in limited observations each year. How-

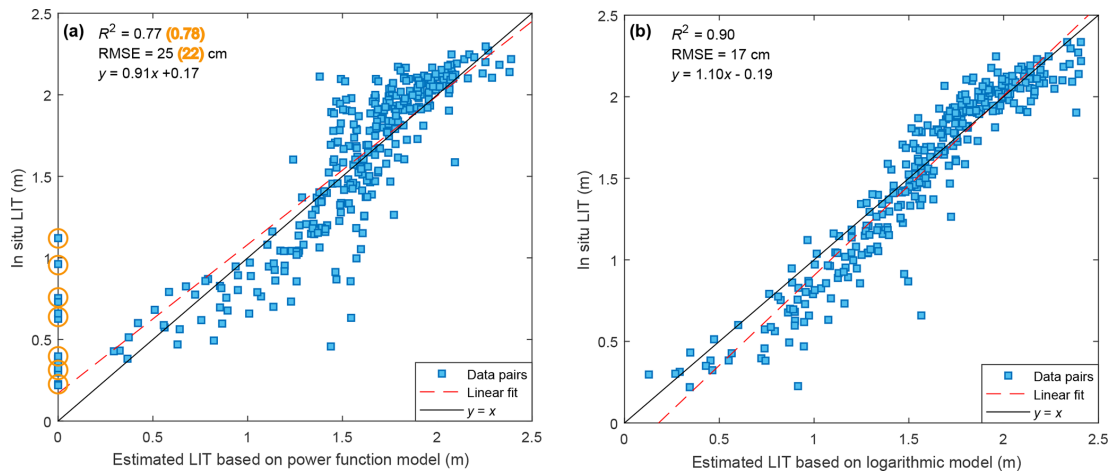


**Figure 6.** Comparison between in situ and estimated LIT of Baker Lake based on (a) a power function model (Zakharova et al., 2021) and (b) a logarithmic model (this study). For both models, a separate set of parameters were derived for each ice season to best fit the in situ LIT. Panels (a) and (b) are scatterplots of all the matched data pairs from 2003 to 2019. Numbers in parentheses denote metrics after the removal of outliers marked by yellow circles.

ever, based on the limited waveform-based LIT, e.g., four or five observations over 0.5 m, the backscattered LIT can be generated to provide more complete tracking of the lake ice thickness, as shown in Fig. 7e. The performance in Lake Peipus is relatively lower in terms of CC, which is likely due to a higher contribution of signals from the lake surface snow, as the snow generally comprises 20 %–50 % of the total thickness.

LITs in GSL and Baker lake are relatively large, and the ice thickness grows rapidly at the beginning of the ice season, making these lakes not suitable for validating thin ice estimates. For Peipus Lake, the LIT is so small that, for many years, there has been no available waveform-based LIT to calibrate parameters for the logarithmic model. To further assess the capability of backscattered LIT in the detection of thinner ice, we compared the altimetry-based LIT with modeled LIT in another two lakes with ice thickness of ~ 1 m, i.e., Hulun (117.38° E 48.97° N) and Har (93.21° E 48.05° N). Given the different advantages of waveform-based LIT and backscattered LIT, we used an empirical method to merge the LIT time series based on waveforms and backscattering coefficients; for waveform-based LIT measurements, we reserved those larger than 0.7 m, and for backscattering-coefficient-based measurements, we reserved those smaller than 0.7 m.

Another reason for selecting the two lakes above is that there is little snowfall in these lakes during ice-covered seasons (as shown in Fig. 8), which can reduce the impact of surface snow because the physical process of surface snow is complicated and could cause large uncertainty in modeled results (Han et al., 2019, 2021). The waveform-based LIT in Hulun Lake was not sufficient to build a regression model (see Sect. 3.2) for each winter before 2014, so we only made a cross-validation through 2014–2018. In Har Lake,

**Table 3.** Validation/cross-validation metrics of altimetry-based LIT in five study lakes.

Lake name	CC	RMSE (cm)	Reference data
Baker Lake	0.94	24	In situ
Great Slave Lake	0.80	17	In situ
Peipus Lake	0.76	11	In situ
Hulun Lake	0.94	11	Modeled
Har Lake	0.89	20	Modeled

the cross-validation was made through 2003–2018, as shown in Fig. 8. Overall, the merged altimetric LIT and model results agree well with each other in terms of an  $R^2$  of 0.88 for Hulun Lake and 0.79 for Har Lake. But there is a relatively larger discrepancy in Har Lake, which is likely caused by the narrower cross-section of Har Lake and fewer available altimetric footprints.

4.3 Water level estimation for ice-covered lakes

The merged LSH time series were obtained by combining the LSH based on the 0.1-threshold and the 0.5-threshold methods, as illustrated in Sect. 3.3. Results in Fig. 9 show that, with the systematic bias during the open-water period removed, the LSH during ice seasons derived from the 0.5 threshold is higher than that derived from the 0.1 threshold, which contradicts the intuition that the 0.5-threshold-based LSH should be lower than the 0.1-threshold-based LSH. It suggests that different choices of thresholds would result in different backscattering interfaces when the lake surface is covered with snow and ice. For instance, Yang et al. (2021) suggested that the 0.1 threshold corresponds to the snow–ice interface, while Li et al. (2022a), using a 0.5 threshold, sug-

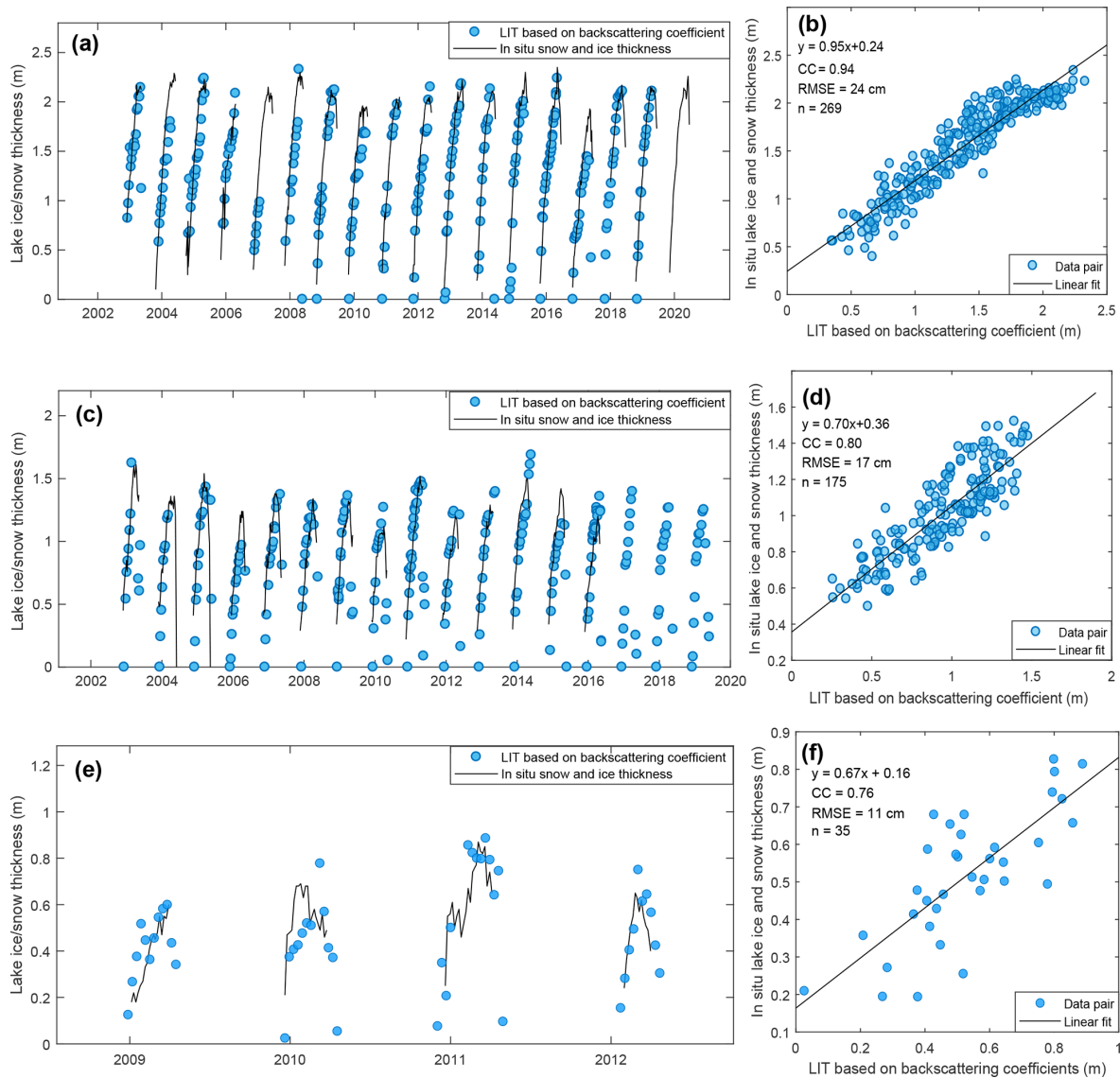


**Figure 7.** Validation of backscattering-coefficient-based LIT against the total thickness of ice and snow. Panels (a), (c), and (e) are time series for the backscattering-coefficient-based LIT and the in situ lake ice and snow thickness in Baker Lake, GSL, and Peipus Lake. Panels (b), (d), and (f) are the scatterplots of backscattering-coefficient-based LITs and in situ lake ice and snow thickness in Baker Lake, GSL, and Peipus Lake, respectively.

gested that their results were close to the air–snow interface. We further discuss causes of this phenomenon in Sect. 5.1, indicating that conclusions from Yang et al. (2021) and Li et al. (2022a) are not contradictory.

When comparing LSH derived from the 0.1 threshold and the 0.5 threshold, we noticed that the 0.5-threshold-based LSH retrievals have a more robust performance during the open-water period (as shown in Fig. S2) and corroborated by previous studies (Davis, 1997). For the ice-covered period, the 0.1-threshold-based LSH retrievals are very close to the hydrostatic water level, as suggested by Yang et al. (2021). Therefore, we merged the two LSH time series (after remov-

ing their systematic bias during open-water periods) by reserving the 0.5-threshold-based LSH during the open-water period and 0.1-threshold-based LSH for the ice-covered period to improve the overall performance of water level estimation. The improvements in the merged LSH time series compared to those based on a single threshold are shown in Table 4.

We derived the altimetric LSH time series for four lakes, namely Athabasca Lake, GBL, GSL, and Winnipeg Lake. Results were validated with in situ water levels using RMSEs (Fig. 10). As mentioned in Sect. 3.3, the LSH time series based on both 0.1 and 0.5 thresholds were derived first



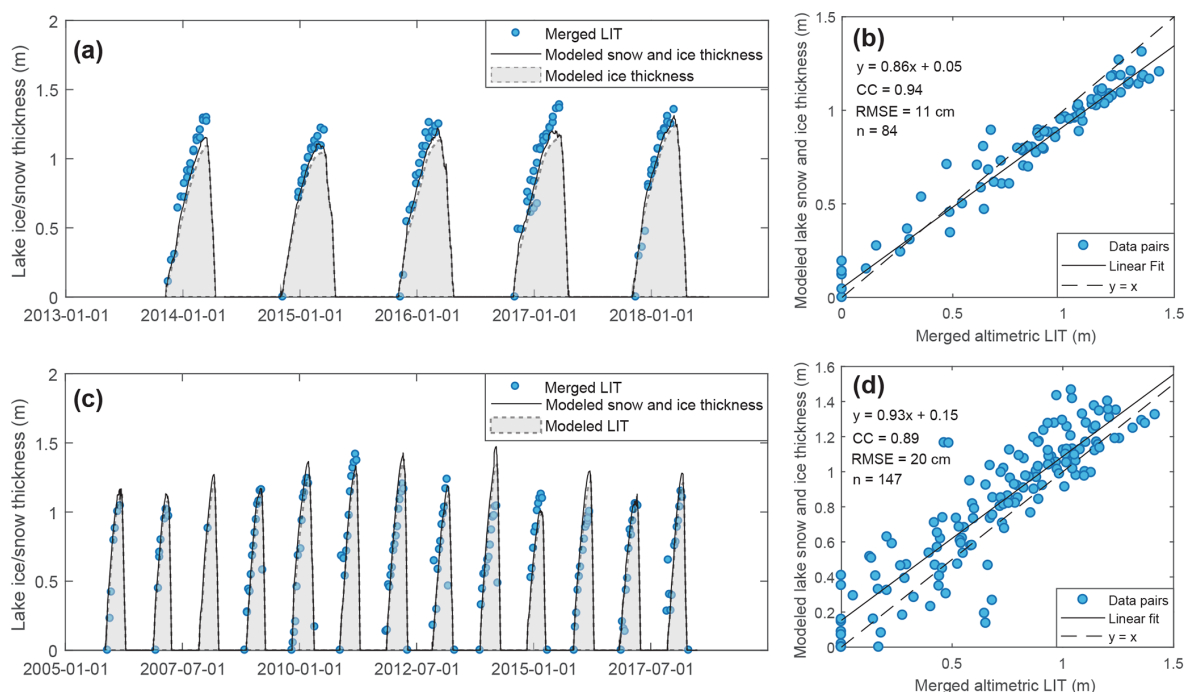


**Figure 8.** Cross-validation between the merged altimetric LIT (waveforms and backscattering-coefficient-based) and modeled lake snow and ice thickness. Panels (a) and (c) are time series for merged altimetric LIT and modeled lake snow and ice for Hulun Lake and Har Lake, where the blue dots denote merged altimetric LIT, shaded areas denote modeled LIT, and black curves denote modeled lake ice and snow thickness. Panels (b) and (d) are scatterplots for altimetric LIT and modeled lake ice and snow thickness for Hulun Lake and Har Lake, respectively.

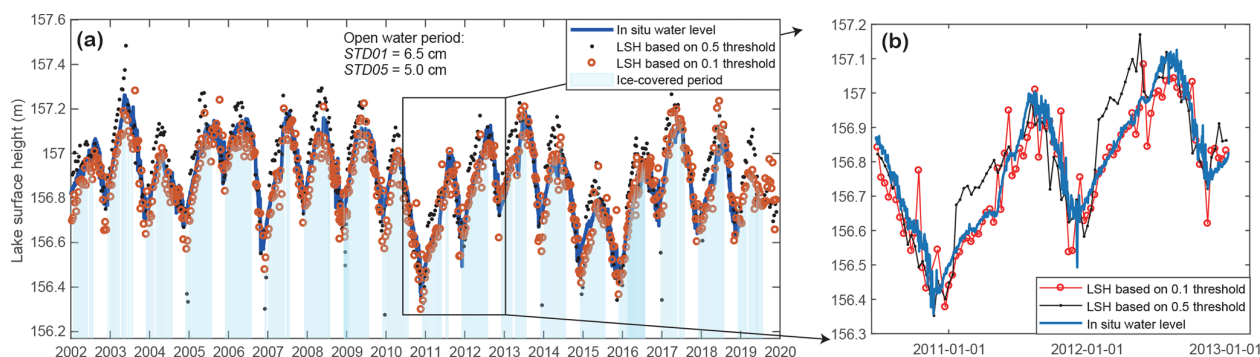


**Figure 9.** Comparison between LSH estimates using different thresholds in GSL. Panel (a) shows time series for altimetric LSH based on different thresholds and in situ water levels. Panel (b) is a magnified view for the LSH time series during 2011–2013. The blue curve denotes in situ water levels, red dots denote LSH based on a 0.1 threshold, black dots denote LSH based on a 0.5 threshold, and light blue shaded areas denote ice-covered seasons.

and then merged into one time series by removing the systematic bias during open-water periods. Compared to in situ measurements, the 0.1-threshold-based LSH retrievals outperformed the 0.5-threshold-based LSH retrievals in representing hydrostatic water levels during ice-covered periods, while the 0.5-threshold-based LSH better represents in situ water levels during open-water periods (Fig. 6). Therefore, the merged LSH time series should outperform both 0.1- and 0.5-threshold-based LSH time series. We did notice an im-

provement of 1.5–2 cm in the RMSE for each lake, as shown in Table 4. Overall, the metrics of the derived water levels are consistent with those from Yang et al. (2021) in GSL, GBL, and Athabasca Lake. However, a direct comparison with metrics from Yang et al. (2021) would be inappropriate, as we used different ground tracks and different gauging stations.



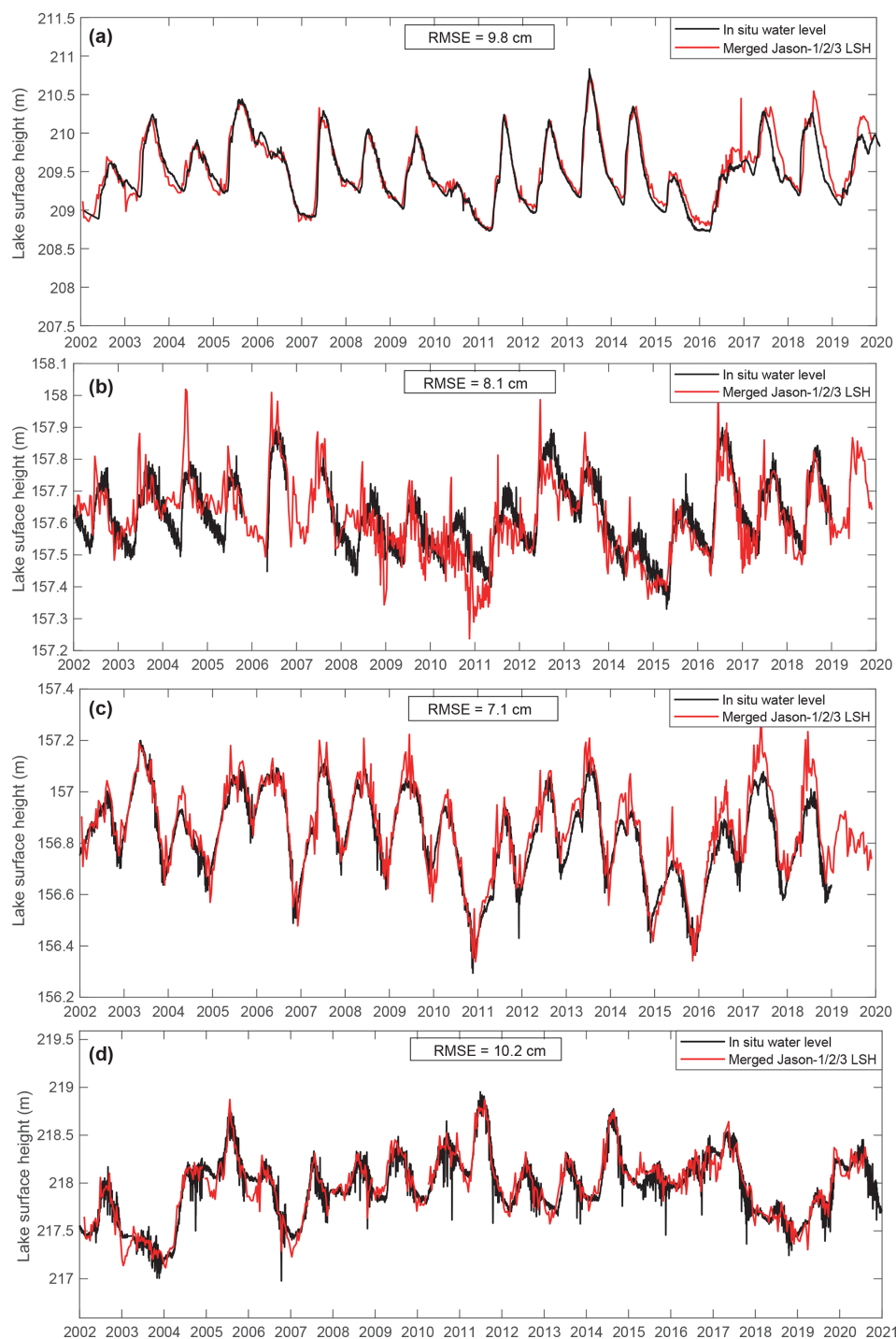


**Figure 10.** Time series of merged altimetric water levels in Athabasca Lake, GBL, GSL, and Winnipeg Lake. Black curves denote in situ lake water levels and red curves denote merged altimetric LSH for (a) Athabasca Lake, (b) GBL, (c) GSL, and (d) Winnipeg Lake. Note that there are systematic biases between Jason-1/2/3 data, which were removed by comparing the mean LSH during the overlapping periods between Jason-1 and Jason-2 (July 2008–January 2009) and Jason-2 and Jason-3 (February–September 2016).

**Table 4.** Improvements in merged LSH compared with the LSH based on a single threshold validated against in situ water levels.

Lake name	Merged LSH RMSE (cm)	0.1-threshold RMSE (cm)	0.5-threshold RMSE (cm)
GSL	7.1	8.0	14
GBL	8.1	9.4	10.6
Athabasca Lake	9.8	11.5	12.5
Winnipeg Lake	10.2	11.7	19.4

## 5 Discussion

### 5.1 Conceptual explanation for differences in LSH derived from different thresholds

Normally a higher threshold of waveform retracking yields a lower LSH, but the comparison shown in Fig. 9 indicates that LSH based on the 0.5 threshold is higher than that based on the 0.1 threshold when the systematic bias during open-water periods is removed. Here we provide a conceptual explanation as to why such a phenomenon occurs. As shown in Fig. 11a–c, the pulse-limited satellite altimetry sends a microwave pulse with a certain width to the open-water surface (with a calm wave surface), and the illuminated area gradually increases to the maximum when the upper bound of the pulse reaches the water surface. Ideally, the largest illuminated area is associated with the peak of the radar waveform (Fig. 11c). For threshold retracking methods, a portion of the maximum power is used to mark the time when the radar pulse reaches the backscattering surface. For instance, the 0.1 threshold method essentially means that the moment when the echoed radar pulse surpasses a 10 % of the waveform peak is selected to be the time when the radar pulse reaches the lake surface (Fig. 11a).

To make the process of the threshold retracking more visible, we assume a sphere within the pulse, as shown by the black dashed curve in Fig. 11. The hypothetical sphere is assumed to have a certain distance/time lag from the lower bound of the radar pulse, and we name it the 0.1 sphere for simplicity. The time when the 0.1 sphere reaches the lake surface indicates that the 0.1 threshold is met and that an LSH is recorded. The recorded LSH is the absolute height of the radar pulse with respect to the reference ellipsoid or geoid (e.g., for Fig. 11a–c, 100, 99.5, and 99 m). Similarly, we assume a sphere for the 0.5-threshold method and name it the 0.5 sphere, as shown by the yellow dashed curve in Fig. 11. For open-water periods, received waveforms only come from the air–water interface, and the time lag (range difference) between the 0.1 sphere and the 0.5 sphere is a relatively stable value with some fluctuations caused by varying wave heights.

When the lake is covered by snow and ice, the illuminated areas become more complicated (Fig. 11d–f). The waveform consists of information from multiple backscattering sur-

faces and volume backscattering. Consequently, there could be multiple peaks in the waveform. Here, we only focus on the first peak because it is most relevant to either the snow surface or snow–ice interface. Based on previous studies (Atwood et al., 2015; Beckers et al., 2017), we assume the first waveform peak to occur when the upper bound of the pulse reaches the snow–ice interface, as shown in Fig. 11f. Then we apply the 0.1- and 0.5-threshold methods to the first peak (Fig. 11d–e). If there is no snow cover and volume scattering, the 0.1 threshold would be met when the 0.1 sphere reaches the ice surface and the 0.5 threshold would be met when the 0.5 sphere reaches the ice surface. However, volume scattering from snow layers contributes to the returned power so that the backscattered energy increases faster than the case without volume scattering. Consequently, the time lag (range difference) between the 0.1 sphere and the 0.5 sphere is compressed. Meanwhile, the LSH recorded in Fig. 11d–f could be 99.6, 99.4, and 98.9 m. The associated systematic bias between the 0.1 threshold (Fig. 11d) and the 0.5 threshold (Fig. 11f) becomes smaller than the case of open water (Fig. 11a–b). Therefore, with the systematic bias during the open-water period removed, the 0.5-threshold-based LSH would be larger than the 0.1-threshold-based LSH in ice-covered seasons.

Here we used the LSH during 2008–2009 in GSL as an example to illustrate the case above. Figure 12 shows the original LSH based on the 0.5-threshold method and the 0.1-threshold method with systematic bias. During the open-water period, the average difference in LSH between the 0.1 threshold and the 0.5 threshold is  $0.46 \pm 0.04$  m, while that during the ice-covered season decreases to  $0.36 \pm 0.02$  m, as shown in Fig. 12. With the system bias during the open-water period removed, the LSH based on 0.5 threshold will inevitably exceed that based on the 0.1 threshold during the ice-covered period.

### 5.2 Uncertainty and limitations

The main source of uncertainty in LIT estimation is lake surface snow cover. As a result of the impact of snow cover, the accuracy of remotely sensed LIT is in general 0.1–0.2 m in current studies. As discussed in Sect. 5.1, lake surface snow could influence radar waveforms and backscattering coefficients. In addition, some physical variables or processes related to snow and ice not considered in our model could also contribute to the uncertainty in the results.

Regarding the backscattered LIT, we did not consider the effect of volume scattering. Volume scattering is caused by snow particles and air bubbles captured inside ice, while ice-bottom scattering is controlled mostly by the roughness and dielectric constant ( $\epsilon$ ) of the ice–water interface. For dry snow, volume scattering from snow cover can increase the backscattering coefficients of Ku-band radar obtained from frozen lakes (Gunn et al., 2015). Based on Kim et al. (1984), thicker snow cover contributes more to backscattering co-

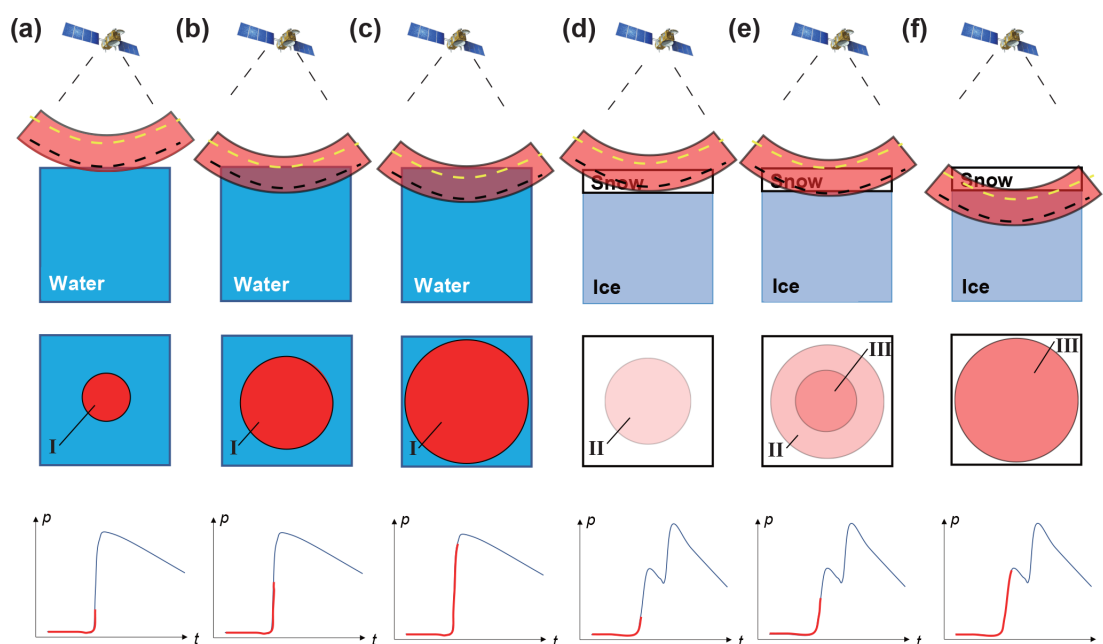


**Figure 11.** A schematic diagram of pulse-limited radar footprints/illuminated areas and associated waveforms on open-water (a–c) and ice-covered (d–f) lakes. The first horizontal panel shows the side view of the radar pulse and backscattering interfaces. Black and yellow dashed curves denote hypothetical spheres within the radar pulse associated with the 0.1 and 0.5 thresholds, respectively. The second horizontal panel represents the illuminated areas in a vertical view, where circular area I denotes backscattering from the water surface (a–c), circular area II denotes backscattering from snow layers (d, e), and circular area III denotes surface backscattering from the snow–ice interface (e, f). The third horizontal panel shows the waveforms associated with illuminated areas in the second panel.  $P$  represents the returned power and  $t$  represents the time/gate. The red curve indicates the part of the waveform that has emerged, whereas the blue curve indicates the rest part. Waveforms in panels (a)–(c) indicate moments when a 10 %, 50 %, and 100 % of the waveform peak is met, respectively. Waveforms in panels (d)–(f) indicate moments when a 10 %, 50 %, and 100 % of the peak in the first subwaveform is met, respectively.

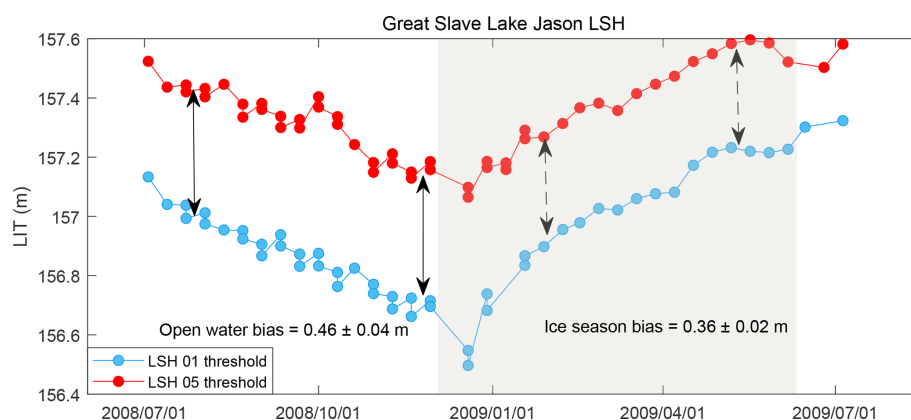


**Figure 12.** Different systematic biases between the LSH based on the 0.1 threshold and the 0.5 threshold in different seasons. Red and blue curves denote original LSH based on the 0.1 threshold and the 0.5 threshold in GSL during 2008–2009. The gray shade represents the ice-covered season.

efficients due to enhanced volume scattering. Consequently, given the same ice condition, backscattering coefficients obtained from thick snow-covered lakes should be larger, which could result in an underestimation of the LIT. On the other hand, wet snow can hardly be penetrated by microwaves and

could largely reduce the backscattered energy, resulting in overestimation of the LIT.

For the waveform-based LIT, the most important physical property is the  $\varepsilon$  of snow and ice, as it determines the speed of light within snow and ice and the timing of reflected signals from different interfaces (higher  $\varepsilon$  corresponds to the lower

speed of light). During the ice accumulation process, the  $\varepsilon$  of ice is relatively stable. The  $\varepsilon$  of dry snow is almost solely dependent on snow density (Tiuri et al., 1984), which can be approximated with  $\varepsilon = 1 + 2\rho$ , where  $\rho$  is the relative snow density (with respect to water). However, we used the same constant  $\varepsilon$  for both ice and snow, which is a compromise, as we do not have any prior information related to snow depth and density. Because the waveform-based method measures the time difference between different interfaces at the beginning of ice and snow accumulation, our method could slightly underestimate the total thickness of snow and ice because snow has a smaller  $\varepsilon$  and a larger speed of light. As the snow becomes denser during the frozen period, and the speed of light becomes slower in snow, the waveform-based LIT could be closer to the total thickness of snow and ice.

As for the uncertainty in water levels, apart from the impact of snow and altimeter range resolution, the source of uncertainty is associated with remaining systematic biases. Water level time series for ice-covered lakes are based on the connection of observations from Jason-1/2/3 after the removal of systematic biases. To identify systematic biases, mean water levels from different sensors during overlapping periods are compared, which is a technique commonly used. However, it is not clear to what extent the remaining systematic biases contribute to the uncertainty in the entire water level series. We estimated that the upper limit of the remaining systematic biases is  $\sim 5$  cm. A detailed description of uncertainty quantification can be found in the Supplement (Sect. S1).

### 5.3 Implications for future studies

Based on the discussion in Sect. 5.1, different thresholds correspond to different interfaces (e.g., air–snow and snow–ice interfaces) in ice-covered seasons. If the estimation of LSH with different threshold methods can be further improved, then it is possible to discriminate the snow depth from the altimetric LIT. The relationship between backscattering coefficients and the surface snow depth can be further investigated, which could facilitate more robust modeling of lake ice and snow based on backscattering coefficients. It could also facilitate more sophisticated validation of lake ice models containing snow processes.

The method developed here has the potential to be used in early satellite altimetry missions, including T/P, ERS-1/2, and some follow-on missions such as Jason-CS (Scharroo et al., 2016), extending remotely sensed LIT to 3 decades and wider spatial coverage. However, it should be investigated whether the developed method is suited for Ka-band altimeters or SAR altimeters such as SARAL/AltiKa, CryoSat-2, and Sentinel-3. This is because the penetration ability of Ka-band microwaves and Ku-band microwaves in ice and snow could be quite different and the pulse-Doppler-limited waveforms (or beam-limited waveforms; e.g., CryoSat-2) are different from pulse-limited waveforms.

## 6 Conclusions

This study presents an effective method to retrieve LIT based solely on altimetric data (including waveforms and backscattering coefficients), which is applicable to lakes without in situ LIT measurements. We also investigate water level estimation for ice-covered lakes by merging LSH time series derived from different threshold retracking algorithms. The major findings are as follows:

1. A logarithmic regression model could be more effective in converting backscattering coefficients into LITs than a previously used power function model (in terms of an  $R^2$  of 0.90 and an RMSE of 17 cm for the developed logarithmic model).
2. When validated against in situ measurements and modeled lake ice and snow thickness, the developed altimetric LIT estimation method combines the advantages from the waveform-based method (physically based and sensitive to thick ice) and the backscattering-coefficient-based method (sensitive to thin ice). The accuracy (or RMSE) of the merged altimetric LIT is  $\sim 0.2$  m for the study lakes.
3. Merging LSH time series derived from different threshold retracking algorithms (0.1 and 0.5 thresholds) can improve the performance of the water level estimation for the entire study period by 1.5–2 cm, compared to the estimation with single threshold methods in terms of RMSE among the study lakes.
4. Different threshold retracking algorithms (0.1 and 0.5 thresholds) can represent different backscattering surfaces for ice-covered lakes. Compared to the same baseline (LSH during the open-water period), the 0.1 threshold could represent the snow–ice interface, while the 0.5 threshold could be closer to the air–snow interface.

Overall, we provide a more robust and adaptive method for the remote sensing of LIT and LSH for ice-covered lakes without in situ observations. The differential impact of lake surface snow on different threshold methods and its implications in future research related to altimetric LIT and water level estimation are discussed. This study facilitates a better interpretation of satellite altimetry signals from ice-covered lakes and provides opportunities for a wider application of altimetry data to the cryosphere.

*Code and data availability.* The data and code presented in this study are available on a reasonable request from the corresponding author.

*Supplement.* The supplement related to this article is available online at: <https://doi.org/10.5194/tc-17-349-2023-supplement>.

**Author contributions.** XL and DL conceptualized the paper and developed the methodology. XL curated the data and prepared the original draft. DL, YC, TL, JL, MAH, and MMM reviewed and edited the paper.

**Competing interests.** The contact author has declared that none of the authors has any competing interests.

**Disclaimer.** Publisher's note: Copernicus Publications remains neutral with regard to jurisdictional claims in published maps and institutional affiliations.

**Acknowledgements.** The comments from the reviewers and editors that helped improve this study and paper are highly appreciated. The authors sincerely thank the Canadian Ice Service, for providing in situ lake ice and snow thickness, the Water Survey of Canada, for providing the in situ water levels, and the AVISO+, for providing the satellite altimetry data that enabled us to conduct this study.

**Financial support.** This research has been supported by the Major Science and Technology Projects of Inner Mongolia Autonomous Region (grant no. 2020ZD0009) and the National Natural Science Foundation of China (grant no. 92047301).

**Review statement.** This paper was edited by Homa Kheyrollah Pour and reviewed by two anonymous referees.

## References

- Abdul Aziz, O. I. and Burn, D. H.: Trends and variability in the hydrological regime of the Mackenzie River Basin, *J. Hydrol.*, 319, 282–294, <https://doi.org/10.1016/j.jhydrol.2005.06.039>, 2006.
- Atwood, D. K., Gunn, G. E., Roussi, C., Wu, J., Duguay, C., and Sarabandi, K.: Microwave backscatter from Arctic lake ice and polarimetric implications, *IEEE T. Geosci. Remote*, 53, 5972–5982, <https://doi.org/10.1109/TGRS.2015.2429917>, 2015.
- Beckers, J. F., Casey, J. A., and Haas, C.: Retrievals of Lake Ice Thickness From Great Slave Lake and Great Bear Lake Using CryoSat-2, *IEEE T. Geosci. Remote*, 55, 3708–3720, <https://doi.org/10.1109/TGRS.2017.2677583>, 2017.
- Cai, Z., Jin, T., Li, C., Ofterdinger, U., Zhang, S., Ding, A., and Li, J.: Is China's fifth-largest inland lake to dry-up? Incorporated hydrological and satellite-based methods for forecasting Hulun lake water levels, *Adv. Water Resour.*, 94, 185–199, <https://doi.org/10.1016/j.advwatres.2016.05.010>, 2016.
- Cheng, B., Mäkynen, M., Similä, M., Rontu, L., and Vihma, T.: Modelling snow and ice thickness in the coastal Kara Sea, Russian Arctic, *Ann. Glaciol.*, 54, 105–113, <https://doi.org/10.3189/2013AoG62A180>, 2013.
- Cooley, S. W., Ryan, J. C., Smith, L. C., Horvat, C., Pearson, B., Dale, B., and Lynch, A. H.: Coldest Canadian Arctic communities face greatest reductions in shorefast sea ice, *Nat. Clim. Change*, 10, 533–538, <https://doi.org/10.1038/s41558-020-0757-5>, 2020.
- Davis, C. H.: A robust threshold retracking algorithm for measuring ice-sheet surface elevation change from satellite radar altimeters, *IEEE T. Geosci. Remote*, 35, 974–979, <https://doi.org/10.1109/36.602540>, 1997.
- Du, J., Kimball, J. S., Duguay, C., Kim, Y., and Watts, J. D.: Satellite microwave assessment of Northern Hemisphere lake ice phenology from 2002 to 2015, *The Cryosphere*, 11, 47–63, <https://doi.org/10.5194/tc-11-47-2017>, 2017.
- Duguay, C. and Lafleur, P.: Determining depth and ice thickness of shallow sub-Arctic lakes using space-borne optical and SAR data, *Int. J. Remote Sens.*, 24, 475–489, <https://doi.org/10.1080/01431160304992>, 2003.
- Duguay, C. R., Flato, G. M., Jeffries, M. O., Menard, P., Morris, K., and Rouse, W. R.: Ice-cover variability on shallow lakes at high latitudes: model simulations and observations, *Hydrol. Process.*, 17, 3465–3483, <https://doi.org/10.1002/hyp.1394>, 2003.
- Engram, M., Anthony, K. W., Sachs, T., Kohnert, K., Serafimovich, A., Grosse, G., and Meyer, F.: Remote sensing northern lake methane ebullition, *Nat. Clim. Change*, 10, 511–517, <https://doi.org/10.1038/s41558-020-0762-8>, 2020.
- Fu, L.-L. and Cazenave, A.: Satellite altimetry and earth sciences: a handbook of techniques and applications, Elsevier, <https://doi.org/10.1029/01EO00233>, 2000.
- Gunn, G. E., Brogioni, M., Duguay, C., Macelloni, G., Kasurak, A., and King, J.: Observation and modeling of X- and Ku-band backscatter of snow-covered freshwater lake ice, *IEEE J. Sel. Top. Appl.*, 8, 3629–3642, 2015.
- Han, P. F., Long, D., Han, Z. Y., Du, M. D., Dai, L. Y., and Hao, X. H.: Improved understanding of snowmelt runoff from the headwaters of China's Yangtze River using remotely sensed snow products and hydrological modeling, *Remote Sens. Environ.*, 224, 44–59, <https://doi.org/10.1016/j.rse.2019.01.041>, 2019.
- Han, Z. Y., Long, D., Han, P. F., Huang, Q., Du, M. D., and Hou, A. Z.: An improved modeling of precipitation phase and snow in the Lancang River Basin in Southwest China, *Sci. China Technol. Sc.*, 64, 1513–1527, <https://doi.org/10.1007/s11431-020-1788-4>, 2021.
- Horstmann, J., Koch, W., Lehner, S., and Tonboe, R.: Wind retrieval over the ocean using synthetic aperture radar with C-band HH polarization, *IEEE T. Geosci. Remote*, 38, 2122–2131, <https://doi.org/10.1109/36.868871>, 2000.
- Horstmann, J., Schiller, H., Schulz-Stellenfleth, J., and Lehner, S.: Global wind speed retrieval from SAR, *IEEE T. Geosci. Remote*, 41, 2277–2286, <https://doi.org/10.1109/tgrs.2003.814658>, 2003.
- Howell, S. E. L., Brown, L. C., Kang, K.-K., and Duguay, C. R.: Variability in ice phenology on Great Bear Lake and Great Slave Lake, Northwest Territories, Canada, from SeaWiFS/QuikSCAT: 2000–2006, *Remote Sens. Environ.*, 113, 816–834, <https://doi.org/10.1016/j.rse.2008.12.007>, 2009a.
- Howell, S. E. L., Brown, L. C., Kang, K.-K., and Duguay, C. R.: Variability in ice phenology on Great Bear Lake and Great Slave Lake, Northwest Territories, Canada, from SeaWiFS/QuikSCAT: 2000–2006, *Remote Sens. Environ.*, 113, 816–834, <https://doi.org/10.1016/j.rse.2008.12.007>, 2009b.
- Howell, S. E. L., Komarov, A. S., Dabboor, M., Montpetit, B., Brady, M., Scharien, R. K., Mahmud, M. S., Nandan, V., Geldsetzer, T., and Yackel, J. J.: Comparing L- and C-band syn-

- thetic aperture radar estimates of sea ice motion over different ice regimes, *Remote Sens. Environ.*, 204, 380–391, <https://doi.org/10.1016/j.rse.2017.10.017>, 2018.
- Howell, S. E. L., Small, D., Rohner, C., Mahmud, M. S., Yackel, J. J., and Brady, M.: Estimating melt onset over Arctic sea ice from time series multi-sensor Sentinel-1 and RADARSAT-2 backscatter, *Remote Sens. Environ.*, 229, 48–59, <https://doi.org/10.1016/j.rse.2019.04.031>, 2019.
- Huang, Q., Long, D., Du, M., Zeng, C., Li, X., Hou, A., and Hong, Y.: An improved approach to monitoring Brahmaputra River water levels using retracked altimetry data, *Remote Sens. Environ.*, 211, 112–128, <https://doi.org/10.1016/j.rse.2018.04.018>, 2018.
- Huang, Q., Li, X. D., Han, P. F., Long, D., Zhao, F. Y., and Hou, A. Z.: Validation and application of water levels derived from Sentinel-3A for the Brahmaputra River, *Sci. China Technol. Sci.*, 62, 1760–1772, <https://doi.org/10.1007/s11431-019-9535-3>, 2019.
- Kang, K.-K., Duguay, C. R., Howell, S. E., Derksen, C. P., and Kelly, R. E.: Sensitivity of AMSR-E brightness temperatures to the seasonal evolution of lake ice thickness, *IEEE Geosci. Remote S.*, 7, 751–755, <https://doi.org/10.1109/LGRS.2010.2044742>, 2010.
- Kang, K. K., Duguay, C. R., Lemmetyinen, J., and Gel, Y.: Estimation of ice thickness on large northern lakes from AMSR-E brightness temperature measurements, *Remote Sens. Environ.*, 150, 1–19, <https://doi.org/10.1016/j.rse.2014.04.016>, 2014.
- Kim, Y.-S., Onstott, R., and Moore, R.: Effect of a snow cover on microwave backscatter from sea ice, *IEEE J. Oceanic Eng.*, 9, 383–388, 1984.
- Knoll, L. B., Sharma, S., Denfeld, B. A., Flaim, G., Hori, Y., Magnuson, J. J., Straile, D., and Weyhenmeyer, G. A.: Consequences of lake and river ice loss on cultural ecosystem services, *Limnol. Oceanogr. Lett.*, 4, 119–131, <https://doi.org/10.1002/lol2.10116>, 2019.
- Kouraev, A. V., Zakharova, E. A., Remy, F., and Suknev, A. Y.: Study of Lake Baikal Ice Cover from Radar Altimetry and In-Situ Observations, *Mar. Geod.*, 38, 477–486, <https://doi.org/10.1080/01490419.2015.1008155>, 2015.
- Kropáček, J., Maussion, F., Chen, F., Hoerz, S., and Hochschild, V.: Analysis of ice phenology of lakes on the Tibetan Plateau from MODIS data, *The Cryosphere*, 7, 287–301, <https://doi.org/10.5194/tc-7-287-2013>, 2013.
- Larue, F., Picard, G., Aublanc, J., Arnaud, L., Robledano-Perez, A., Le Meur, E., Favier, V., Jourdain, B., Savarino, J., and Thibaut, P.: Radar altimeter waveform simulations in Antarctica with the Snow Microwave Radiative Transfer Model (SMRT), *Remote Sens. Environ.*, 263, 112534, <https://doi.org/10.1016/j.rse.2021.112534>, 2021.
- Li, X., Long, D., Huang, Q., Han, P., Zhao, F., and Wada, Y.: High-temporal-resolution water level and storage change data sets for lakes on the Tibetan Plateau during 2000–2017 using multiple altimetric missions and Landsat-derived lake shoreline positions, *Earth Syst. Sci. Data*, 11, 1603–1627, <https://doi.org/10.5194/essd-11-1603-2019>, 2019.
- Li, X., Long, D., Huang, Q., and Zhao, F.: Supplementary Data for “The state and fate of lake ice thickness in the Northern Hemisphere”, Zenodo [data set], <https://doi.org/10.5281/zenodo.5528542>, 2021.
- Li, X., Long, D., Huang, Q., and Zhao, F.: The state and fate of lake ice thickness in the Northern Hemisphere, *Sci. Bull.*, 67, 537–546, <https://doi.org/10.1016/j.scib.2021.10.015>, 2022a.
- Li, X., Long, D., Scanlon, B. R., Mann, M. E., Li, X., Tian, F., Sun, Z., and Wang, G.: Climate change threatens terrestrial water storage over the Tibetan Plateau, *Nat. Clim. Change*, 12, 801–807, <https://doi.org/10.1038/s41558-022-01443-0>, 2022b.
- Long, D. and Li, X.: Water loss over the Tibetan Plateau endangers water supply security for Asian populations, *Nat. Clim. Change*, 12, 785–786, <https://doi.org/10.1038/s41558-022-01451-0>, 2022.
- Mangilli, A., Thibaut, P., Duguay, C. R., and Murfitt, J.: A New Approach for the Estimation of Lake Ice Thickness From Conventional Radar Altimetry, *IEEE T. Geosci. Remote*, 60, 1–15, 2022.
- Medeiros, A. S., Friel, C. E., Finkelstein, S. A., and Quinlan, R.: A high resolution multi-proxy record of pronounced recent environmental change at Baker Lake, Nunavut, *J. Paleolimnol.*, 47, 661–676, <https://doi.org/10.1007/s10933-012-9589-2>, 2012.
- Mullan, D., Swindles, G., Patterson, T., Galloway, J., Macumber, A., Falck, H., Crossley, L., Chen, J., and Pisarcic, M.: Climate change and the long-term viability of the World’s busiest heavy haul ice road, *Theor. Appl. Climatol.*, 129, 1089–1108, <https://doi.org/10.1007/s00704-016-1830-x>, 2017.
- Murfitt, J. and Duguay, C. R.: 50 years of lake ice research from active microwave remote sensing: Progress and prospects, *Remote Sens. Environ.*, 264, 112616, <https://doi.org/10.1016/j.rse.2021.112616>, 2021.
- Murfitt, J., Duguay, C. R., Picard, G., and Gunn, G. E.: Investigating the Effect of Lake Ice Properties on Multifrequency Backscatter Using the Snow Microwave Radiative Transfer Model, *IEEE T. Geosci. Remote*, 60, 1–23, 2022.
- Murfitt, J. C., Brown, L. C., and Howell, S. E. L.: Estimating lake ice thickness in Central Ontario, *PLOS ONE*, 13, e0208519, <https://doi.org/10.1371/journal.pone.0208519>, 2018.
- Peureux, C., Longépé, N., Mouche, A., Tison, C., Tourain, C., Lachiver, J. m., and Hauser, D.: Sea-ice detection from near-nadir Ku-band echoes from CFOSAT/SWIM scatterometer, *Earth Space Sci.*, 9, e2021EA002046, <https://doi.org/10.1029/2021EA002046>, 2022.
- Pour, H. K., Duguay, C. R., Scott, K. A., and Kang, K.-K.: Improvement of lake ice thickness retrieval from MODIS satellite data using a thermodynamic model, *IEEE T. Geosci. Remote*, 55, 5956–5965, 2017.
- Scharroo, R., Bonekamp, H., Ponsard, C., Parisot, F., von Engeln, A., Tahtadjiev, M., de Vriendt, K., and Montagner, F.: Jason continuity of services: continuing the Jason altimeter data records as Copernicus Sentinel-6, *Ocean Sci.*, 12, 471–479, <https://doi.org/10.5194/os-12-471-2016>, 2016.
- Sharma, S., Blagrove, K., Magnuson, J. J., O’Reilly, C. M., Oliver, S., Batt, R. D., Magee, M. R., Straile, D., Weyhenmeyer, G. A., and Winslow, L.: Widespread loss of lake ice around the Northern Hemisphere in a warming world, *Nat. Clim. Change*, 9, 227–231, <https://doi.org/10.1038/s41558-018-0393-5>, 2019.
- Sharma, S., Blagrove, K., Watson, S. R., O’Reilly, C. M., Batt, R., Magnuson, J. J., Clemens, T., Denfeld, B. A., Flaim, G., and Grinberga, L.: Increased winter drownings in ice-covered regions with warmer winters, *PLOS ONE*, 15, e0241222, <https://doi.org/10.1371/journal.pone.0241222>, 2020.



- Shu, S., Liu, H., Beck, R. A., Frappart, F., Korhonen, J., Xu, M., Yang, B., Hinkel, K. M., Huang, Y., and Yu, B.: Analysis of Sentinel-3 SAR altimetry waveform retracking algorithms for deriving temporally consistent water levels over ice-covered lakes, *Remote Sens. Environ.*, 239, 111643, <https://doi.org/10.1016/j.rse.2020.111643>, 2020.
- Stewardship, M. W.: State of Lake Winnipeg: 1999 to 2007, Environment Canada and Manitoba Water Stewardship, ISBN 978-1-100-18827-0, 2011.
- Tiuri, M., Sihvola, A., Nyfors, E., and Hallikaiken, M.: The complex dielectric constant of snow at microwave frequencies, *IEEE J. Ocean. Eng.*, 9, 377–382, 1984.
- Wang, W., Lee, X., Xiao, W., Liu, S., Schultz, N., Wang, Y., Zhang, M., and Zhao, L.: Global lake evaporation accelerated by changes in surface energy allocation in a warmer climate, *Nat. Geosci.*, 11, 410–414, <https://doi.org/10.1038/s41561-018-0114-8>, 2018.
- Warren, S. G. and Brandt, R. E.: Optical constants of ice from the ultraviolet to the microwave: A revised compilation, *J. Geophys. Res.-Atmos.*, 113, D14220, <https://doi.org/10.1029/2007JD009744>, 2008.
- Wik, M., Varner, R. K., Anthony, K. W., MacIntyre, S., and Bastviken, D.: Climate-sensitive northern lakes and ponds are critical components of methane release, *Nat. Geosci.*, 9, 99–105, <https://doi.org/10.1038/ngeo2578>, 2016.
- Woolway, R. I., Kraemer, B. M., Lenters, J. D., Merchant, C. J., O'Reilly, C. M., and Sharma, S.: Global lake responses to climate change, *Nature Reviews Earth & Environment*, 1, 388–403, <https://doi.org/10.1038/s43017-020-0067-5>, 2020.
- Wu, Q., Li, C., Sun, B., Shi, X., Zhao, S., and Han, Z.: Change of ice phenology in the Hulun Lake from 1986 to 2017, *Prog. Geogr.*, 38, 1933–1943, <https://doi.org/10.18306/dlkxjz.2019.12.009>, 2019.
- Wu, Y., Long, D., Lall, U., Scanlon, B. R., Tian, F., Fu, X., Zhao, J., Zhang, J., Wang, H., and Hu, C.: Reconstructed eight-century streamflow in the Tibetan Plateau reveals contrasting regional variability and strong nonstationarity, *Nat. Commun.*, 13, 6416, <https://doi.org/10.1038/s41467-022-34221-9>, 2022.
- Yang, X., Pavelsky, T. M., and Allen, G. H.: The past and future of global river ice, *Nature*, 577, 69–73, <https://doi.org/10.1038/s41586-019-1848-1>, 2020.
- Yang, Y., Moore, P., Li, Z., and Li, F.: Lake Level Change From Satellite Altimetry Over Seasonally Ice-Covered Lakes in the Mackenzie River Basin, *IEEE T. Geosci. Remote*, 59, 8143–8152, <https://doi.org/10.1109/tgrs.2020.3040853>, 2021.
- Yu, Y. and Rothrock, D.: Thin ice thickness from satellite thermal imagery, *J. Geophys. Res.-Oceans*, 101, 25753–25766, 1996.
- Zakharova, E., Agafonova, S., Duguay, C., Frolova, N., and Kouraev, A.: River ice phenology and thickness from satellite altimetry: potential for ice bridge road operation and climate studies, *The Cryosphere*, 15, 5387–5407, <https://doi.org/10.5194/tc-15-5387-2021>, 2021.
- Zeng, T., Shi, L., Marko, M., Cheng, B., Zou, J., and Zhang, Z.: Sea ice thickness analyses for the Bohai Sea using MODIS thermal infrared imagery, *Acta Ocean. Sin.*, 35, 96–104, <https://doi.org/10.1007/s13131-016-0908-8>, 2016.
- Zhang, G., Ran, Y., Wan, W., Luo, W., Chen, W., Xu, F., and Li, X.: 100 years of lake evolution over the Qinghai–Tibet Plateau, *Earth Syst. Sci. Data*, 13, 3951–3966, <https://doi.org/10.5194/essd-13-3951-2021>, 2021.
- Zhao, F., Long, D., Li, X., Huang, Q., and Han, P.: Rapid glacier mass loss in the Southeastern Tibetan Plateau since the year 2000 from satellite observations, *Remote Sens. Environ.*, 270, 112853, <https://doi.org/10.1016/j.rse.2021.112853>, 2022.
- Ziyad, J., Goita, K., Magagi, R., Blarel, F., and Frappart, F.: Improving the Estimation of Water Level over Freshwater Ice Cover using Altimetry Satellite Active and Passive Observations, *Remote Sensing*, 12, 967, <https://doi.org/10.3390/rs12060967>, 2020.